Chemotactic Motility-Induced Phase Separation

Hongbo Zhao[ORCID],[1] Andrej Košmrlj[ORCID],[2,3] and Sujit S. Datta[ORCID][1,*]

[1]*Department of Chemical and Biological Engineering, Princeton University, Princeton, New Jersey 08544, USA*
[2]*Department of Mechanical and Aerospace Engineering, Princeton University, Princeton, New Jersey 08544, USA*
[3]*Princeton Materials Institute, Princeton University, Princeton, New Jersey 08544, USA*

Collectives of actively moving particles can spontaneously separate into dilute and dense phases—a fascinating phenomenon known as motility-induced phase separation (MIPS). MIPS is well-studied for randomly moving particles with no directional bias. However, many forms of active matter exhibit collective chemotaxis, directed motion along a chemical gradient that the constituent particles can generate themselves. Here, using theory and simulations, we demonstrate that collective chemotaxis strongly competes with MIPS—in some cases, arresting or completely suppressing phase separation, or in other cases, generating fundamentally new dynamic instabilities. We establish principles describing this competition, thereby helping to reveal and clarify the rich physics underlying active matter systems that perform chemotaxis, ranging from cells to robots.

The thermodynamics of active matter—collections of agents that consume energy to move or exert forces—has been studied extensively due to its fundamental richness as well as its importance to diverse applications [1,2]. One prominent class of active matter is that composed of self-propelled agents, ranging from enzymes [3–5] and cells [6–9] to synthetic microswimmers and robots [10–12]. These forms of active matter can often be modeled as collections of active Brownian particles (ABPs), each of which self-propels with a velocity of magnitude U_0 and a direction that is continually reoriented by random thermal fluctuations, eventually decorrelating over a timescale τ_R. The persistence length of an ABP trajectory is then given by $\sim U_0 \tau_R$; the directedness of a particle of radius a can therefore be described by the reorientation Péclet number $\mathrm{Pe}_R \equiv a/(U_0 \tau_R)$.

Studies of this canonical model have led to fascinating insights into the thermodynamics of active matter. For example, phase separation in passive equilibrium systems typically requires attractive interactions between constituents; in stark contrast, for small Pe_R, ABPs undergo motility-induced phase separation (MIPS) into dense and dilute phases without attractive interactions [13–18]. Remarkably, this nonequilibrium process can often be described using models inspired by the phase separation of thermally equilibrated passive systems [15,19–22].

This prior work focused on ABPs that move randomly, with no preferred direction. However, many forms of active matter exhibit collective *chemotaxis*—directed motion in response to an external chemical gradient that can be generated collectively by the agents themselves. In biology, this phenomenon enables populations of cells to escape from harmful environments, colonize new terrain, and

migrate as groups [6,23–32]; at the subcellular level, enzymes may also perform chemotaxis [3–5]. Synthetic active materials that can perform chemotaxis have also been developed, often exhibiting new surprises in their phase behavior—e.g., unusual clustering and oscillatory density fluctuations [10,11,33–42]. However, despite these hints that chemotaxis can influence the physics of active matter, a broader understanding of how exactly chemotaxis alters MIPS remains lacking.

Here, we address this gap in knowledge by developing a theoretical model that combines both MIPS and chemotaxis, which are usually studied in isolation. We find that collective chemotaxis can dramatically suppress MIPS, arrest phase separation, or engender new complex phase separation dynamics reminiscent of other pattern-forming systems [43–59], but that arise due to completely different physics—in this case, due to the competition between MIPS, which drives ABPs to cluster into dense phases, and chemotaxis, which instead drives them to disperse away.

Governing equations.—Building on existing continuum models of MIPS [15,19–22], we describe the time evolution of the volume fraction ϕ of *chemotactic* ABPs via the continuity equation

$$\frac{\partial \phi}{\partial t} = -\nabla \cdot \boldsymbol{J}, \tag{1}$$

$$\boldsymbol{J} = \underbrace{-M_0 \phi \nabla \left(\tilde{\mu}_h(\phi, \mathrm{Pe}_R) - \kappa \nabla^2 \phi \right)}_{\text{MIPS}} + \underbrace{\chi_0 \phi \nabla f(\tilde{c})}_{\text{chemotaxis}}, \tag{2}$$

where t is time and $\boldsymbol{J}$ is the flux of particles. This flux has two contributions, as indicated by the underbraces in

Eq. (2). The first reflects active Brownian motion, as established by the classical "model B"; in future work, it would be interesting to explore other models of MIPS that treat additional complexities [20]. As detailed in Sec. 1 of [60], $M_0 = 0.5U_0^2\tau_R$ is the active diffusivity reflecting the random undirected motion of the particles, $\tilde{\mu}_h$ is the bulk chemical potential nondimensionalized by the energy scale $0.5\zeta U_0^2\tau_R$ with drag coefficient ζ, and the characteristic length scale $\sqrt{\kappa} \sim U_0\tau_R$ sets the width of the interface between the dense and dilute phases in MIPS [15,19].

The second term in Eq. (2) represents a new addition of chemotaxis to this classical model of MIPS. This term is widely used to describe the chemotaxis of microorganisms [6,24–32,77] as well as many synthetic forms of active matter [4,34,78,79]; indeed, it can be directly derived from an explicit microscopic description of chemotactic ABPs as detailed in Sec. 2 of [60], based on [34]. Here, $\tilde{c}$ is the concentration, nondimensionalized by a fixed characteristic concentration, of a diffusible chemical signal (the "chemoattractant") that the particles sense and direct their motion in response to. The monotonically increasing function $f(\tilde{c})$ describes the ability of the particles to sense the chemoattractant; we take $f(\tilde{c}) = \tilde{c}$ as an illustrative example [80,81]. The chemotactic coefficient χ_0 describes the ability of the particles to move up the sensed chemoattractant gradient. Thus, $\chi_0\nabla f(\tilde{c})$ describes the chemotactic velocity, and when multiplied by ϕ describes the chemotactic flux [82,83]. Hence, we define a new chemotactic Péclet number $\text{Pe}_C \equiv \chi_0/M_0$ to describe the competition between directed chemotaxis and undirected active diffusion.

Chemoattractants (e.g., nutrients) are often taken up by the particles themselves—thereby collectively generating a local chemoattractant gradient that the particles bias their motion in response to [24–26,28,34,37,39,40,84–88]. Thus, we describe the chemoattractant via

$$\frac{\partial \tilde{c}}{\partial t} = D_c\nabla^2\tilde{c} - k\phi g(\tilde{c}) + S, \qquad (3)$$

where D_c is the chemoattractant diffusivity, k is the characteristic volumetric rate of chemoattractant uptake, and $g(\tilde{c})$ describes how uptake rate increases with $\tilde{c}$; we use the linearized $g(\tilde{c}) = \tilde{c}$ for simplicity. Finally, S represents the rate at which chemoattractant is externally supplied, taken to be constant and spatially uniform as an illustrative example.

Chemotaxis suppresses MIPS.—First, we establish the conventional case of MIPS as a baseline, described by our governing Eqs. (1)–(3) with $\text{Pe}_C = 0$. To do so, we choose a functional form for $\tilde{\mu}_h(\phi, \text{Pe}_R)$, given by Eq. (S4) of [60], that derives from a previously established ABP equation of state [16,89]. The homogeneous state with constant, spatially uniform $\phi(\mathbf{x}) = \phi_0$, where $\mathbf{x}$ denotes position, becomes unstable to fluctuations in ϕ when the free energy is nonconvex ($\partial_\phi\tilde{\mu}_h < 0$). Therefore, the spinodal curve

demarcating the limit of stability is given by $\partial_\phi\tilde{\mu}_h = 0$, shown by the black curves in Fig. 1; ϕ_0 represents the ABP volume fraction averaged over the entire system. Above this spinodal curve, the homogeneous state is linearly stable. Below the spinodal, ABPs spontaneously separate into dense and dilute phases, initially forming domains with a most unstable wavelength $\sim q_{\text{sp}}^{-1} \equiv \sqrt{-2\kappa/\partial_\phi\tilde{\mu}_h}$ that coarsen over time via spinodal decomposition (Movie S1) as established previously [19,89].

How do the features of MIPS change upon the introduction of chemotaxis ($\text{Pe}_C > 0$)? Given a constant and uniform S, the homogeneous state is now described by spatially uniform ABP and chemoattractant profiles, $\phi(\mathbf{x}) = \phi_0$ and $\tilde{c}(\mathbf{x}) = \tilde{c}_0$, where $\tilde{c}_0$ is given by the steady-state solution to Eq. (3), $\tilde{c}_0 = S/(k\phi_0)$. By perturbing this steady state with small-amplitude fluctuations $\delta\phi = \delta\hat{\phi}e^{i\mathbf{q}\cdot\mathbf{x}+\omega t}$ and $\delta\tilde{c} = \delta\hat{c}e^{i\mathbf{q}\cdot\mathbf{x}+\omega t}$ of spatial wave vector $\mathbf{q}$ and growth rate ω, we obtain the dispersion relation $\omega(q)$, given by Eq. (S33) of [60], where $q = |\mathbf{q}|$ is the wave number of a given mode. The homogeneous state is linearly stable if $\text{Re}\,\omega < 0$, which is always true when $\partial_\phi\tilde{\mu}_h > 0$. We therefore focus our subsequent analysis on the spinodal region of nonchemotactic MIPS where $\partial_\phi\tilde{\mu}_h < 0$, and nondimensionalize $\mathbf{q}$ and ω by the characteristic nonchemotactic MIPS quantities q_{sp} and $\omega_{\text{sp}} \equiv \omega(q_{\text{sp}}; \text{Pe}_C = 0)$.

As detailed in Sec. 3 of [60], the dispersion relation for chemotactic MIPS [Eq. (S37)] solely depends on three dimensionless parameters: $\alpha \equiv -M_0\phi_0\partial_\phi\tilde{\mu}_h/D_c$, which compares the collective ABP diffusivity $-M_0\phi_0\partial_\phi\tilde{\mu}_h$ to that of the chemoattractant; the Damköhler number $\text{Da} \equiv k\phi_0/(2D_cq_{\text{sp}}^2) = -\kappa k\phi_0/(D_c\partial_\phi\tilde{\mu}_h)$, which compares the rates of chemoattractant uptake and diffusion over the length scale $q_{\text{sp}}^{-1}/\sqrt{2}$; and the reduced chemotactic Péclet number $\text{Pe}_C' \equiv \chi_0\tilde{c}_0/(-M_0\phi_0\partial_\phi\tilde{\mu}_h)$. Because the MIPS phase diagram is conventionally parametrized by ϕ_0 and Pe_R, which together set $\partial_\phi\tilde{\mu}_h$ [Eq. (S5)], we also define versions of the three dimensionless parameters that are independent of these variables: $\alpha_0 \equiv M_0/D_c$, $\text{Da}_0 \equiv \kappa k/D_c$, and Pe_C given earlier, such that $\alpha = -\alpha_0\phi_0\partial_\phi\tilde{\mu}_h$, $\text{Da} = -\text{Da}_0\phi_0/\partial_\phi\tilde{\mu}_h$, and $\text{Pe}_C' = -\text{Pe}_C \cdot S/(k\phi_0^2\partial_\phi\tilde{\mu}_h)$. Furthermore, because the proportionality between Pe_C' and Pe_C is scaled by S/k, without loss of generality, we fix the chemoattractant supply rate $S/k = 1$. Chemotactic MIPS is then parametrized by a total of five governing parameters: $\{\phi_0, \text{Pe}_R, \alpha_0, \text{Da}_0, \text{Pe}_C\}$, as summarized in Table S1. Thus, to examine how chemotaxis influences MIPS, we first investigate how the conventional $\phi_0 - \text{Pe}_R$ phase diagram of MIPS changes upon varying α_0, Da_0, and Pe_C.

As detailed in Sec. 3 of [60] and summarized in Appendix A, our first main result from the linear stability analysis is that phase separation is suppressed by chemotaxis, but only when two criteria are *simultaneously* satisfied: (i) $\text{Pe}_C' \geq \text{Pe}_{C\text{crit}}'$, and (ii) $\alpha \leq \alpha_{\text{crit}}$, where $\text{Pe}_{C\text{crit}}' = (1+\min\{\text{Da},1\})^2/(4\cdot\min\{\text{Da},1\})$ and $\alpha_{\text{crit}} = 1 + 2\cdot\text{Da} + 2\sqrt{\text{Da}(1+\text{Da})}$. We therefore designate the limits given by
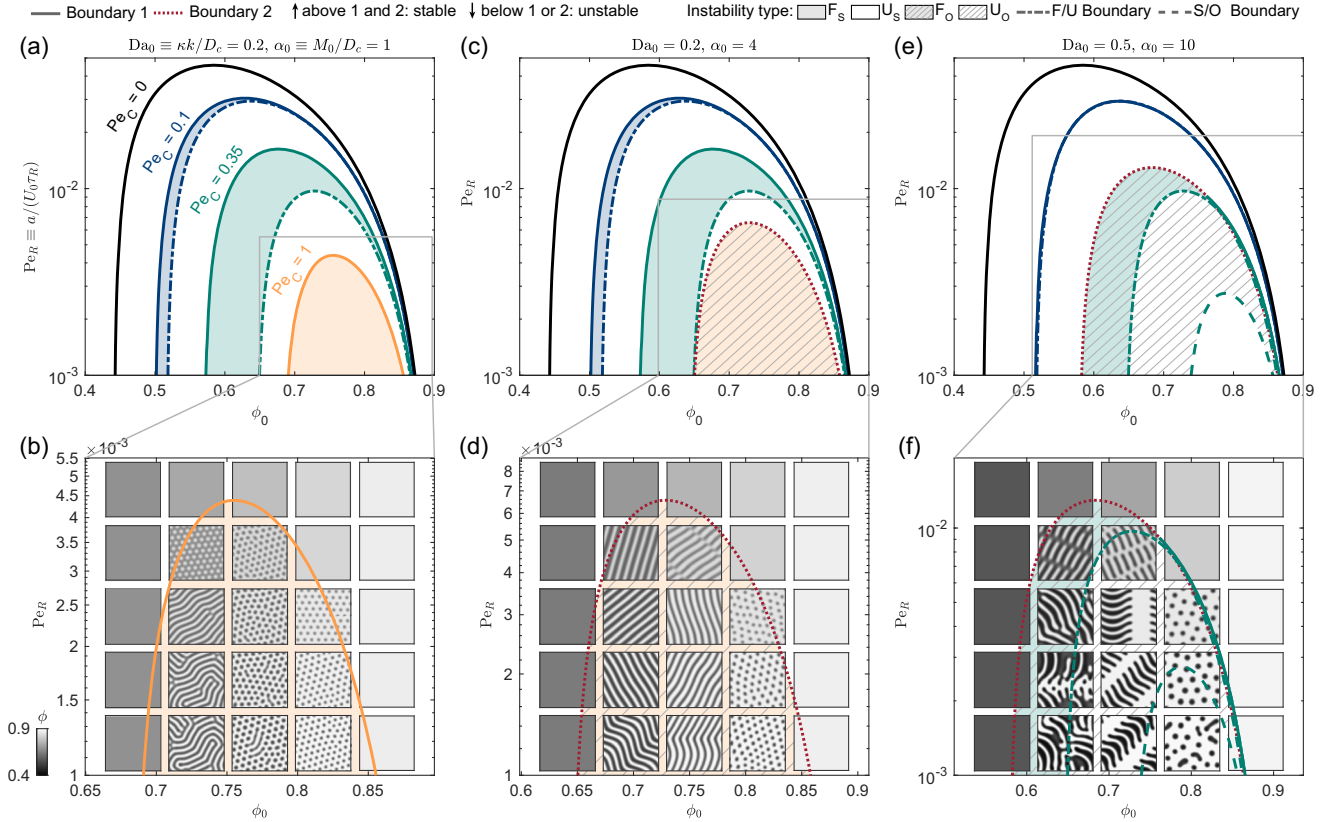
FIG. 1. Chemotaxis suppresses MIPS. (a),(c),(e) Phase diagram determined by linear stability analysis for different Da_0 and α_0; ϕ_0 represents the system-averaged ABP volume fraction. The black curve shows the limit of stability without chemotaxis, below which is conventional MIPS. The colored solid and red dotted curves show Boundaries 1 and 2, defined in the main text; different colors indicate different Pe_C. Boundary 2 is below the horizontal axis in (a). The region above *both* boundaries is stable (ABPs in the homogeneous state), while the region below *either* boundary is unstable. The different instability types—finite (F) or unbounded (U), stationary (S) or oscillatory (O)—are denoted by the shaded, unshaded, nonhashed, and hashed regions, respectively. Dash-dotted and dashed curves indicate the boundaries between F/U and S/O instabilities, respectively. The predictions are corroborated by simulations (Movies S2-S4), snapshots of which are shown in (b),(d),(f), which focus on the gray boxed regions shown in (a),(c),(e). Snapshots in (b) and (d) correspond to $Pe_C = 1$, while $Pe_C = 0.35$ in (f).

$Pe_C' = Pe_{C\mathrm{crit}}'$ and $\alpha = \alpha_{\mathrm{crit}}$ as "Boundary 1" and "Boundary 2"—shown in the $Pe_R - \phi_0$ phase diagrams (Fig. 1) by the solid and red dotted curves, respectively. Boundary 1 is colored by the different values of Pe_C. Boundary 2 does not depend on Pe_C. Criteria (i) and (ii) correspond to the regions above Boundaries 1 and 2, respectively; hence, the region above *both* boundaries represents the stable regime in which the ABPs are in the homogeneous state, while conversely, the region below *either* Boundary 1 *or* 2 represents the unstable regime in which the ABPs phase separate.

As a starting example, we consider $Da_0 = 0.2$ and $\alpha_0 = 1$, shown in Fig. 1(a). In this case, Boundary 2 is below the horizontal axis; hence, the system is linearly stable above Boundary 1 and unstable below it. Boundary 1 shifts to lower Pe_R and a narrower range of ϕ_0 with increasing Pe_C. That is, the region of instability shrinks and phase separation is suppressed when chemotaxis is stronger. Numerical simulations at $Pe_C = 1$ confirm this linear stability result: ABPs are in the homogeneous state above Boundary 1, but

phase separate below it, as shown in Fig. 1(b). Intriguingly, the features of this phase separation appear to be fundamentally distinct from the spinodal decomposition observed in conventional nonchemotactic MIPS. For example, as shown in Movie S2, ABPs phase separate into finite-sized domains that remain stationary and do not subsequently coarsen—unlike in conventional MIPS.

Next, upon increasing α_0 to 4, Boundary 1 remains unaltered, but Boundary 2 shifts upward, as shown in Fig. 1(c). As a result, for the case of $Pe_C = 1$, Boundary 2 rises above Boundary 1, which is omitted since Boundary 2 now corresponds to the limit of stability, as confirmed by numerical simulations shown in Fig. 1(d). As shown in Movie S3, ABPs phase separate into finite-sized domains and bands that form traveling waves, a feature that is fundamentally distinct both from conventional MIPS and Fig. 1(b).

Finally, to highlight yet another distinct form of phase separation, we then increase both α_0 and Da_0 in Fig. 1(e),

where Boundary 1 shifts downward while Boundary 2 shifts upward, part of which becomes the limit of stability for $\mathrm{Pe}_C = 0.35$, confirmed by simulations in Fig. 1(f). Strikingly, we find that throughout the unstable region, the patterns vary from traveling bands that are extended (shaded green + hashed region) or less extended (unshaded + hashed region) to domains that stretch, rotate, and translate (unshaded region below the green dashed curve), as shown in Movie S4.

Taken altogether, these results demonstrate that MIPS is suppressed when (1) the strength of chemotaxis, as quantified by Pe_C, *and* (2) chemoattractant diffusivity relative to that of the ABPs, as quantified by α_0^{-1}, are sufficiently high. Moreover, our simulations reveal that the features of phase separation are dramatically altered by chemotaxis—with separated domains that initially can either be finite-sized or unbounded in space, and can either be stationary or exhibit complex oscillatory dynamics in time, depending on the values of $\{\phi_0, \mathrm{Pe}_R, \alpha_0, \mathrm{Da}_0, \mathrm{Pe}_C\}$. We summarize these results in the $\alpha_0 - \mathrm{Pe}_C$ phase diagram shown in Fig. 2, holding ϕ_0, Pe_R, and Da_0 fixed, and show the region of stability (which lies above Boundary 1 and to the left of Boundary 2 in the $\alpha_0 - \mathrm{Pe}_C$ plane shown) and snapshots of these different types of instability (animated in Movie S5) that we now seek to categorize.
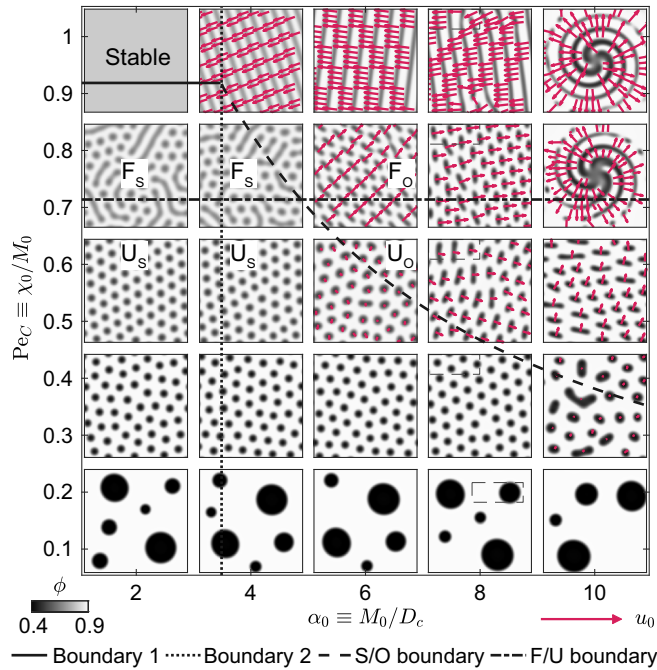

FIG. 2. Chemotaxis arrests phase separation and generates dynamic instabilities. Phase diagram is parametrized by α_0 and Pe_C, holding $\phi_0 = 0.8$, $\mathrm{Pe}_R = 10^{-3}$, and $\mathrm{Da}_0 = 0.5$ fixed. Different instability types predicted by our linear stability analysis are indicated using the same labels as in Fig. 1, again corroborated by simulations (Movie S5), snapshots of which are shown. Arrows show the local velocity field $\boldsymbol{u}$ relative to the characteristic velocity $u_0 \equiv M_0/\sqrt{\kappa} \sim U_0$; $|\boldsymbol{u}| < 0.005 u_0$ vectors are omitted for clarity.

Chemotaxis arrests phase separation.—We first classify the instabilities by their distinct spatial characteristics. In particular, depending on the range of initially unstable wave numbers $q_- < q < q_+$ in the dispersion relation $\omega(q)$ [Eq. (S33)] derived using our linear stability analysis, we differentiate instabilities as being either finite wavelength (F) when the unstable modes are spatially bounded ($q_- > 0$), and therefore phase-separated domains do not coarsen, or unbounded (U) when the unstable modes can instead extend indefinitely in space ($q_- = 0$) [90]. While conventional MIPS is a Type U instability [19,43,89], our second main result is that chemotaxis can give rise to Type F instabilities as well—as shown by the domains that do not coarsen in, e.g., Movies S2 and S3 noted earlier. Comparing the ABP (Movies S2 and S3) and chemoattractant (Movies S6 and S7) profiles reveals the underlying reason: ABPs in an extended, dense domain collectively establish a strong local chemoattractant gradient through uptake—which in turn causes them to bias their motion up the gradient and disperse away, arresting phase separation.

This behavior is also reflected in the simulations shown in Fig. 2 and Movie S5. For the example of $\alpha_0 = 2$ (left of Boundary 2), as Pe_C increases, the coarsening slows and eventually becomes arrested (Sec. 6 of [60]), forming finite-sized domains and stripes—ultimately reaching the homogeneous state at the largest Pe_C above Boundary 1. Examining the dispersion relations corroborates this observation (see Appendix B). Indeed, determining q_- directly from the dispersion relation yields the criterion that Type F is $\mathrm{Pe}'_C > 1$ (shaded regions in Fig. 1), while Type U is given by $\mathrm{Pe}'_C < 1$ (unshaded). The boundary between the two, given by $\mathrm{Pe}'_C = 1$ [Eq. (S68)], is represented by the dash-dotted curves in Figs. 1 and 2. In all cases, our predictions agree well with the simulations, as detailed in Sec. 7 of [60] —thereby providing a description of how chemotaxis can arrest MIPS. Indeed, as described in Sec. 9 of [60], this description may help to rationalize previous observations of bacterial populations [7,91].

Chemotaxis engenders complex oscillatory dynamics.—We further classify the instabilities by their distinct temporal characteristics [43]: "Stationary" (S) if all unstable modes are nonoscillatory with $\mathrm{Im}\,\omega = 0$, or "Oscillatory" (O) if there exist unstable and oscillatory modes with $\mathrm{Re}\,\omega(q) > 0$ and $\mathrm{Im}\,\omega(q) \neq 0$. While conventional MIPS is a Type S instability, our third main result is that chemotaxis can give rise to Type O instabilities as well —e.g., Movies S3 and S4 noted earlier. This behavior is also reflected in Fig. 2 and Movie S5, and is again corroborated by examining the dispersion relations for the example of $\alpha_0 = 8$ (Appendix B). In this case, at large Pe_C, chemotaxis proceeds more rapidly and the diffusing chemoattractant cannot equilibrate fast enough. As a result, variations in $\tilde{c}(\boldsymbol{x})$ lag behind $\phi(\boldsymbol{x})$ (Appendix B), driving sustained large-scale motion of the phase-separated

domains [92,93], e.g., through stretching, rotating, and translating, as indicated by the arrows in Fig. 2 showing the local velocity field $\boldsymbol{u}$.

The dispersion relation again yields a criterion for the Type O instability, shown as the hashed regions in Fig. 1. The Type S/O boundary [Eq. (S60)] is represented using the dashed curves in Figs. 1(e), 1(f) and 2; in Fig. 1(c) and 1(d), this boundary coincides with Boundary 2. We again observe good agreement between the predicted Type S/O boundary and the simulations [94]. Thus, our analysis provides a key first step toward explaining how the interplay between chemotaxis and chemoattractant diffusion can generate more complex phase separation dynamics than in conventional MIPS. Indeed, as described in Sec. 9 of [60], our results may help guide new experiments using synthetic materials [12,95–101] to explore these rich physics. Our simulations also show other complex features, e.g., the quasiordered lattices in Fig. 2, whose description will require nonlinearities to be explicitly incorporated in the analysis; moreover, while here we examined a specific type of chemotaxis and MIPS, our theoretical framework can be readily extended to other forms of taxis and phase separation. We further describe these useful directions for future work in Sec. 10 of [60].

Appendix A: Linear stability analysis.—Here, we provide a summary of the linear stability analysis in Sec. 3 of [60]. Substituting the small-amplitude perturbations $\delta\phi$ and $\delta\tilde{c}$ into linearized Eqs. (1), (2), and (3) yields

$$\omega\delta\hat{\phi} = -M_0\phi_0 q^2(\partial_\phi\tilde{\mu}_h + \kappa q^2)\delta\hat{\phi} + \chi_0\phi_0 q^2 f'(\tilde{c}_0)\delta\hat{c}, \quad (A1)$$

$$\omega\delta\hat{c} = -D_c q^2\delta\hat{c} - k(g(\tilde{c}_0)\delta\hat{\phi} + \phi_0 g'(\tilde{c}_0)\delta\hat{c}). \quad (A2)$$

Section 3E of [60] shows that the system is always linearly stable outside the spinodal region $\partial_\phi\tilde{\mu}_h > 0$. Therefore, we analyze the linear stability when $\partial_\phi\tilde{\mu}_h < 0$ below. Nondimensionalizing the wave number q and growth rate ω via $\tilde{q} = q/(\sqrt{2}q_{sp})$ and $\tilde{\omega} = \omega/(4\omega_{sp})$, we obtain the following quadratic equation for $\tilde{\omega}$:

$$\tilde{\omega}^2 + \left[\tilde{q}^4 - \left(1 - \frac{1}{\alpha}\right)\tilde{q}^2 + \frac{\text{Da}}{\alpha}\right]\tilde{\omega}$$
$$+ \frac{\tilde{q}^2}{\alpha}\left((\tilde{q}^2 - 1)(\tilde{q}^2 + \text{Da}) + \text{Da}\cdot\text{Pe}'_C\right) = 0. \quad (A3)$$

The stability condition is that the two solutions to the equation satisfy $\text{Re}\,\tilde{\omega}_\pm(\tilde{q}) \leq 0$ for all $\tilde{q}$, or equivalently $\tilde{\omega}_+\tilde{\omega}_- > 0$ and $\tilde{\omega}_+ + \tilde{\omega}_- < 0$.

Since

$$\tilde{\omega}_+\tilde{\omega}_- = \frac{\tilde{q}^2}{\alpha}\left((\tilde{q}^2 - 1)(\tilde{q}^2 + \text{Da}) + \text{Da}\cdot\text{Pe}'_C\right), \quad (A4)$$

when $\text{Da} \leq 1$, $\alpha\tilde{q}^{-2}\tilde{\omega}_+\tilde{\omega}_- \geq \text{Da}\cdot(\text{Pe}'_C - 1)$. When $\text{Da} > 1$, $\alpha\tilde{q}^{-2}\tilde{\omega}_+\tilde{\omega}_- \geq -[(1+\text{Da})^2/4] + \text{Da}\cdot\text{Pe}'_C$. Therefore, $\tilde{\omega}_+\tilde{\omega}_- > 0$ for all $\tilde{q}$ is equivalent to criterion (i) ($\text{Pe}'_C \geq \text{Pe}'_{C\text{crit}}$).

Since

$$\tilde{\omega}_+ + \tilde{\omega}_- = -\tilde{q}^4 + \left(1 - \frac{1}{\alpha}\right)\tilde{q}^2 - \frac{\text{Da}}{\alpha}, \quad (A5)$$

when $\alpha \leq 1$, $\tilde{\omega}_+ + \tilde{\omega}_- \leq -\text{Da}/\alpha < 0$. When $\alpha > 1$, $\tilde{\omega}_+ + \tilde{\omega}_- \leq (1 - \alpha^{-1})^2/4 - \text{Da}/\alpha$. Therefore, $\tilde{\omega}_+ + \tilde{\omega}_- < 0$ for all $\tilde{q}$ is equivalent to criterion (ii) ($\alpha \leq \alpha_{\text{crit}}$).

In the main text, we define Type U instability to be when the lower bound of the unstable wave number q_- is zero. As shown in Sec. 3C of [60], this condition is equivalent to requiring that the second order derivative of $\tilde{\omega}_+$ at $\tilde{q} = 0$ is positive, that is, $\tilde{\omega}''_+(\tilde{q} = 0) = 2(1 - \text{Pe}'_C) > 0$, or $\text{Pe}'_C < 1$.

Oscillatory instability emerges when there exists $\tilde{q}$ for which $\text{Re}\,\sigma(\tilde{q}) > 0$ and $\text{Im}\,\sigma(\tilde{q}) \neq 0$, or equivalently $\tilde{\omega}_+\tilde{\omega}_- > 0$ and the discriminant of Eq. (A3) is negative. The first condition requires that criterion (ii) is not satisfied ($\alpha > \alpha_{\text{crit}}$). For the second condition, because the discriminant is

$$\Delta = \left[\tilde{q}^4 - \left(1 + \frac{1}{\alpha}\right)\tilde{q}^2 - \frac{\text{Da}}{\alpha}\right]^2 - \frac{4\text{Da}\cdot\text{Pe}'_C}{\alpha}\tilde{q}^2, \quad (A6)$$

Δ becomes negative when Pe'_C is sufficiently large. Sec. 3D of [60] derives the expression for the critical Pe'_C above which both conditions are met.

Appendix B: The role of chemotaxis in arresting phase separation and generating complex dynamics.— As shown in Fig. 2 and Movie S5, for the example of $\alpha_0 = 2$ (left of Boundary 2), chemotaxis arrests phase separation with increasing Pe_C. Examining the dispersion relations in Fig. 3(a) corroborates this observation. At low nonzero Pe_C, the unstable modes extend to $q_- = 0$ (blue to green curves), indicating a Type U instability. By contrast, for the larger $\text{Pe}_C = 0.75$, $q_- > 0$ (chartreuse curve), indicating a Type F instability.

Also as shown in Fig. 2 and Movie S5, for the example of $\alpha_0 = 8$ (right of Boundary 2), chemotaxis arrests phase separation with increasing Pe_C. Examining the dispersion relations in Fig. 3(b) corroborates this observation. At low Pe_C (blue and cyan curves), all unstable modes (with $\text{Re}\,\omega > 0$) are stationary (having $\text{Im}\,\omega = 0$), indicating a Type S instability; by contrast, at higher Pe_C (green to orange curves), some unstable modes have $\text{Im}\,\omega \neq 0$, indicating a Type O instability.
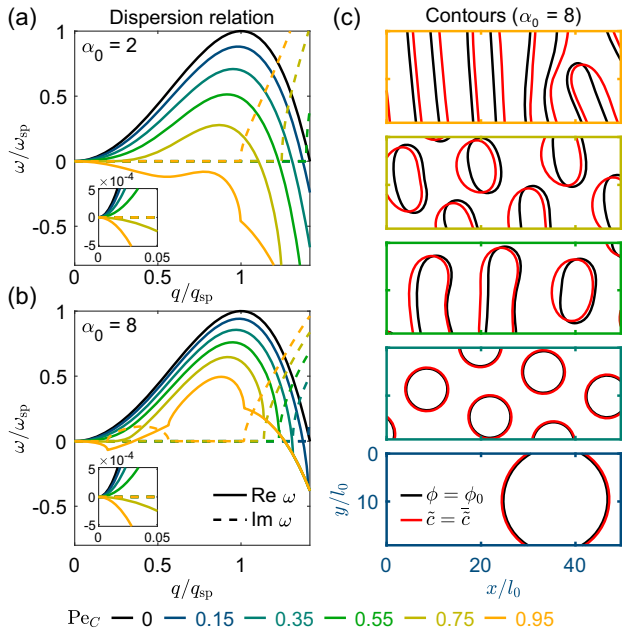
FIG. 3. (a),(b) Dispersion relations $\omega(q)$ corresponding to $\alpha_0 = 2$ and $\alpha_0 = 8$ in Fig. 2; solid (dashed) lines show the Real (Imaginary) components. Insets show long wavelengths. (c) Magnified contours of $\phi = \phi_0$ and $\tilde{c} = \bar{\tilde{c}}$ (the spatial average of $\tilde{c}$) for the dashed rectangles in the snapshots of Fig. 2 at $\alpha_0 = 8$. Different colors in (a)–(c) show the different Pe_C corresponding to the simulations shown in Fig. 2.

Comparing the ABP and chemoattractant profiles, $\phi(\boldsymbol{x})$ and $\tilde{c}(\boldsymbol{x})$ respectively, sheds light on the physics underlying these complex dynamics at large Pe_C and α_0. Figure 3(c) shows the illustrative case of $\alpha_0 = 8$ for the five different Pe_C shown in (a). For the lowest two Pe_C, chemotaxis is weak, enabling $\tilde{c}(\boldsymbol{x})$ to equilibrate in response to changes in $\phi(\boldsymbol{x})$. Consequently, the phase-separated patterns remain stationary, reflective of a Type S instability. For larger Pe_C, however, chemotaxis proceeds more rapidly and the diffusing chemoattractant cannot equilibrate fast enough. As a result, variations in $\tilde{c}(\boldsymbol{x})$ lag behind $\phi(\boldsymbol{x})$, driving directed large-scale motion of the phase-separated domains [92,93], reflective of a Type O instability.

[*]Corresponding author: ssdatta@princeton.edu

[1] M. C. Marchetti, J. F. Joanny, S. Ramaswamy, T. B. Liverpool, J. Prost, M. Rao, and R. A. Simha, Hydrodynamics of soft active matter, Rev. Mod. Phys. **85**, 1143 (2013).

[2] G. Gompper *et al.*, The 2020 motile active matter roadmap, J. Phys. Condens. Matter **32**, 193001 (2020).

[3] F. Mohajerani, X. Zhao, A. Somasundar, D. Velegol, and A. Sen, A theory of enzyme chemotaxis: From experiments to modeling, Biochemistry **57**, 6256 (2018).

[4] J. Agudo-Canalejo, P. Illien, and R. Golestanian, Phoresis and enhanced diffusion compete in enzyme chemotaxis, Nano Lett. **18**, 2711 (2018).

[5] A. Y. Jee, Y. K. Cho, S. Granick, and T. Tlusty, Catalytic enzymes are active matter, Proc. Natl. Acad. Sci. U.S.A. **115**, E10812 (2018).

[6] J. D. Murray, *Mathematical Biology: I. An Introduction* (Springer Science and Business Media, New York, 2007).

[7] G. Liu, A. Patch, F. Bahar, D. Yllanes, R. D. Welch, M. C. Marchetti, S. Thutupalli, and J. W. Shaevitz, Self-Driven Phase Transitions Drive Myxococcus Xanthus Fruiting Body Formation, Phys. Rev. Lett. **122**, 248102 (2019).

[8] R. Alert and X. Trepat, Physical models of collective cell migration, Annu. Rev. Condens. Matter Phys. **11**, 77 (2019).

[9] E. Scarpa and R. Mayor, Collective cell migration in development, J. Cell Biol. **212**, 143 (2016).

[10] J. Palacci, S. Sacanna, A. P. Steinberg, D. J. Pine, and P. M. Chaikin, Living crystals of light-activated colloidal surfers, Science **339**, 936 (2013).

[11] I. Theurkauff, C. Cottin-Bizonne, J. Palacci, C. Ybert, and L. Bocquet, Dynamic Clustering in Active Colloidal Suspensions with Chemical Signaling, Phys. Rev. Lett. **108**, 268303 (2012).

[12] S. Palagi and P. Fischer, Bioinspired microrobots, Nat. Rev. Mater. **3**, 113 (2018).

[13] G. S. Redner, M. F. Hagan, and A. Baskaran, Structure and Dynamics of a Phase-Separating Active Colloidal Fluid, Phys. Rev. Lett. **110**, 055701 (2013).

[14] Y. Fily and M. C. Marchetti, Athermal Phase Separation of Self-Propelled Particles with No Alignment, Phys. Rev. Lett. **108**, 235702 (2012).

[15] M. E. Cates and J. Tailleur, Motility-induced phase separation, Annu. Rev. Condens. Matter Phys. **6**, 219 (2015).

[16] S. C. Takatori and J. F. Brady, Towards a thermodynamics of active matter, Phys. Rev. E **91**, 032117 (2015).

[17] M. E. Cates and J. Tailleur, When are active brownian particles and run-and-tumble particles equivalent? consequences for motility-induced phase separation, Europhys. Lett. **101**, 20010 (2013).

[18] J. Bialké, H. Löwen, and T. Speck, Microscopic theory for the phase separation of self-propelled repulsive disks, Europhys. Lett. **103**, 30008 (2013).

[19] J. Stenhammar, A. Tiribocchi, R. J. Allen, D. Marenduzzo, and M. E. Cates, Continuum Theory of Phase Separation Kinetics for Active Brownian Particles, Phys. Rev. Lett. **111**, 145702 (2013).

[20] E. Tjhung, C. Nardini, and M. E. Cates, Cluster Phases and Bubbly Phase Separation in Active Fluids: Reversal of the Ostwald Process, Phys. Rev. X **8**, 031080 (2018).

[21] T. Speck, J. Bialke, A. M. Menzel, and H. Lowen, Effective Cahn-Hilliard Equation for the Phase Separation of Active Brownian Particles, Phys. Rev. Lett. **112**, 218304 (2014).

[22] M. E. Cates, D. Marenduzzo, I. Pagonabarraga, and J. Tailleur, Arrested phase separation in reproducing bacteria creates a generic route to pattern formation, Proc. Natl. Acad. Sci. U.S.A. **107**, 11715 (2010).

[23] H. C. Berg, Chemotaxis in bacteria :-:9050, Annu. Rev. Biophys. Bioeng. **4**, 119 (1975).

[24] J. Cremer, T. Honda, Y. Tang, J. Wong-ng, M. Vergassola, and T. Hwa, Chemotaxis as a navigation strategy to boost range expansion, Nature (London) **575**, 658 (2019).

[25] X. Fu, S. Kato, J. Long, H. H. Mattingly, C. He, D. C. Vural, S. W. Zucker, and T. Emonet, Spatial self-organization resolves conflicts between individuality and collective migration, Nat. Commun. **9**, 2177 (2018).

[26] T. Bhattacharjee, D. B. Amchin, J. A. Ott, F. Kratz, and S. S. Datta, Chemotactic migration of bacteria in porous media, Biophys. J. **120**, 3483 (2021).

[27] T. Bhattacharjee, D. B. Amchin, R. Alert, J. A. Ott, and S. S. Datta, Chemotactic smoothing of collective migration, eLife **11**, e71226 (2022).

[28] Y. Bai, C. He, P. Chu, J. Long, X. Li, and X. Fu, Spatial modulation of individual behaviors enables an ordered structure of diverse phenotypes during bacterial group migration, eLife **10**, e67316 (2021).

[29] M. Seyrich, A. Palugniok, and H. Stark, Traveling concentration pulses of bacteria in a generalized Keller-Segel model, New J. Phys. **21**, 103001 (2019).

[30] S. Gude, E. Pinçe, K. M. Taute, A. B. Seinen, T. S. Shimizu, and S. J. Tans, Bacterial coexistence driven by motility and spatial competition, Nature (London) **578**, 588 (2020).

[31] J. Saragosti, V. Calvez, N. Bournaveas, A. Buguin, P. Silberzan, and B. Perthame, Mathematical description of bacterial traveling pulses, PLoS Comput. Biol. **6**, e1000890 (2010).

[32] J. A. Moore-Ott, S. Chiu, D. B. Amchin, T. Bhattacharjee, and S. S. Datta, A biophysical threshold for biofilm formation, eLife **11**, e76380 (2022).

[33] H. Stark, Artificial chemotaxis of self-phoretic active colloids: Collective behavior, Acc. Chem. Res. **51**, 2681 (2018).

[34] O. Pohl and H. Stark, Dynamic Clustering and Chemotactic Collapse of Self-Phoretic Active Particles, Phys. Rev. Lett. **112**, 238303 (2014).

[35] B. Liebchen and H. Löwen, Synthetic chemotaxis and collective behavior in active matter, Acc. Chem. Res. **51**, 2982 (2018).

[36] B. Liebchen, D. Marenduzzo, I. Pagonabarraga, and M. E. Cates, Clustering and Pattern Formation in Chemorepulsive Active Colloids, Phys. Rev. Lett. **115**, 258301 (2015).

[37] B. Liebchen, D. Marenduzzo, and M. E. Cates, Phoretic Interactions Generically Induce Dynamic Clusters and Wave Patterns in Active Colloids, Phys. Rev. Lett. **118**, 268001 (2017).

[38] B. Liebchen and D. Levis, Collective Behavior of Chiral Active Matter: Pattern Formation and Enhanced Flocking, Phys. Rev. Lett. **119**, 058002 (2017).

[39] S. Saha, R. Golestanian, and S. Ramaswamy, Clusters, asters, and collective oscillations in chemotactic colloids, Phys. Rev. E **89**, 062316 (2014).

[40] S. Saha, S. Ramaswamy, and R. Golestanian, Pairing, waltzing and scattering of chemotactic active colloids, New J. Phys. **21**, 063006 (2019).

[41] L. Varga, A. Libal, C. J. O. Reichhardt, and C. Reichhardt, Active regimes for particles on resource landscapes, Phys. Rev. Res. **4**, 013061 (2022).

[42] L. Varga, A. Libal, C. Reichhardt, and C. J. O. Reichhardt, Pattern formation and flocking for particles near the jamming transition on resource gradient substrates, Phys. Rev. E **106**, 064602 (2022).

[43] M. C. Cross and P. C. Hohenberg, Pattern formation outside of equilibrium, Rev. Mod. Phys. **65**, 851 (1993).

[44] S. Kondo and T. Miura, Reaction-diffusion model as a framework for understanding biological pattern formation, Science **329**, 1616 (2010).

[45] M. Bär, R. Großmann, S. Heidenreich, and F. Peruani, Self-propelled rods: Insights and perspectives for active matter, Annu. Rev. Condens. Matter Phys. **11**, 441 (2020).

[46] D. Zwicker, A. A. Hyman, and F. Julicher, Suppression of Ostwald ripening in active emulsions, Phys. Rev. E **92**, 012317 (2015).

[47] D. Zwicker, R. Seyboldt, C. A. Weber, A. A. Hyman, and F. Jülicher, Growth and division of active droplets provides a model for protocells, Nat. Phys. **13**, 408 (2017).

[48] A. M. Menzel and H. Lowen, Traveling and Resting Crystals in Active Systems, Phys. Rev. Lett. **110**, 055702 (2013).

[49] A. Ziepke, I. Maryshev, I. S. Aranson, and E. Frey, Multi-scale organization in communicating active matter, Nat. Commun. **13**, 6727 (2022).

[50] S. Saha, J. Agudo-Canalejo, and R. Golestanian, Scalar Active Mixtures: The Nonreciprocal Cahn-Hilliard Model, Phys. Rev. X **10**, 041009 (2020).

[51] Z. You, A. Baskaran, and M. C. Marchetti, Nonreciprocity as a generic route to traveling states, Proc. Natl. Acad. Sci. U.S.A. **117**, 19767 (2020).

[52] J. van der Kolk, F. Rasshofer, R. Swiderski, A. Haldar, A. Basu, and E. Frey, Anomalous Collective Dynamics of Auto-Chemotactic Populations, Phys. Rev. Lett. **131**, 088201 (2023).

[53] R. Matas-Navarro, R. Golestanian, T. B. Liverpool, and S. M. Fielding, Hydrodynamic suppression of phase separation in active suspensions, Phys. Rev. E **90**, 032304 (2014).

[54] R. M. Navarro and S. M. Fielding, Clustering and phase behaviour of attractive active particles with hydrodynamics, Soft Matter **11**, 7525 (2015).

[55] S. Yin and L. Mahadevan, Contractility-induced phase separation in active solids, arXiv:2211.09995.

[56] M. Z. Bazant, Thermodynamic stability of driven open systems and control of phase separation by electro-autocatalysis, Faraday Discuss. **199**, 423 (2017).

[57] R. Adkins, I. Kolvin, Z. You, S. Witthaus, M. C. Marchetti, and Z. Dogic, Dynamics of active liquid interfaces, Science **377**, 768 (2022).

[58] A. M. Tayar, F. Caballero, T. Anderberg, O. A. Saleh, M. C. Marchetti, and Z. Dogic, Controlling liquid-liquid phase behavior with an active fluid, arXiv:2208.12769.

[59] F. Caballero and M. C. Marchetti, Activity-Suppressed Phase Separation, Phys. Rev. Lett. **129**, 268002 (2022).

[60] See Supplemental Material at http://link.aps.org/supplemental/10.1103/PhysRevLett.131.118301, which includes Refs. [61–76], for supplementary details, discussion, and captions of movies.

[61] J. Tailleur and M. E. Cates, Statistical Mechanics of Interacting Run-and-Tumble Bacteria, Phys. Rev. Lett. **100**, 218103 (2008).

[62] L. Shampine and M. Reichelt, Ode matlab solvers, J. Sci. Comput. **18**, 1 (1997).

[63] H. Furukawa, Spinodal decomposition of two-dimensional fluid mixtures: A spectral analysis of droplet growth, Phys. Rev. E **61**, 1423 (2000).

[64] M. Laradji, S. Toxvaerd, and O. G. Mouritsen, Molecular Dynamics Simulation of Spinodal Decomposition in Three-Dimensional Binary Fluids, Phys. Rev. Lett. **77**, 2253 (1996).

[65] S. Mao, D. Kuldinow, M. P. Haataja, and A. Košmrlj, Phase behavior and morphology of multicomponent liquid mixtures, Soft Matter **15**, 1297 (2019).

[66] A. J. Bray, Theory of phase-ordering kinetics, Adv. Phys. **51**, 481 (2002).

[67] M. E. Cates, Diffusive transport without detailed balance in motile bacteria: Does microbiology need statistical physics?, Rep. Prog. Phys. **75**, 042601 (2012).

[68] I. Buttinoni, G. Volpe, F. Kummel, G. Volpe, and C. Bechinger, Active Brownian motion tunable by light, J. Phys. Condens. Matter **24**, 284129 (2012).

[69] J. Stenhammar, R. Wittkowski, D. Marenduzzo, and M. E. Cates, Light-induced self-assembly of active rectification devices, Sci. Adv. **2**, 1 (2016).

[70] J. Arlt, V. A. Martinez, A. Dawson, T. Pilizota, and W. C. Poon, Painting with light-powered bacteria, Nat. Commun. **9**, 1 (2018).

[71] G. Frangipane, D. Dell'Arciprete, S. Petracchini, C. Maggi, F. Saglimbeni, S. Bianchi, G. Vizsnyiczai, M. L. Bernardini, and R. di Leonardo, Dynamic density shaping of photokinetic e. coli, eLife **7**, 1 (2018).

[72] E. F. Keller and L. A. Segel, Initiation of slime mold aggregation viewed as an instability, J. Theor. Biol. **26**, 399 (1970).

[73] E. Sesé-Sansa, I. Pagonabarraga, and D. Levis, Velocity alignment promotes motility-induced phase separation, Europhys. Lett. **124**, 30004 (2018).

[74] M. N. V. D. Linden, L. C. Alexander, D. G. Aarts, and O. Dauchot, Interrupted Motility Induced Phase Separation in Aligning Active Colloids, Phys. Rev. Lett. **123**, 098001 (2019).

[75] A. Wysocki, R. G. Winkler, and G. Gompper, Propagating interfaces in mixtures of active and passive Brownian particles, New J. Phys. **18**, 123030 (2016).

[76] J. Zhang, R. Alert, J. Yan, N. S. Wingreen, and S. Granick, Active phase separation by turning towards regions of higher density, Nat. Phys. **17**, 961 (2021).

[77] R. Alert, A. Martínez-Calvo, and S. S. Datta, Cellular Sensing Governs the Stability of Chemotactic Fronts, Phys. Rev. Lett. **128**, 148101 (2022).

[78] H. Masoud and M. J. Shelley, Collective Surfing of Chemically Active Particles, Phys. Rev. Lett. **112**, 128304 (2013).

[79] B. Liebchen and A. K. Mukhopadhyay, Interactions in active colloids, J. Phys. Condens. Matter **34**, 083002 (2022).

[80] M. P. Brenner, L. S. Levitov, and E. O. Budrene, Physical mechanisms for chemotactic pattern formation by bacteria, Biophys. J. **74**, 1677 (1998).

[81] M. A. Herrero and J. J. L. Velázquez, Chemotactic collapse for the Keller-Segel model, J. Math. Biol. **35**, 177 (1996).

[82] E. F. Keller and L. A. Segel, Model for chemotaxis, J. Theor. Biol. **30**, 225 (1971).

[83] E. F. Keller and L. A. Segel, Traveling bands of chemotactic bacteria: A theoretical analysis, J. Theor. Biol. **30**, 235 (1971).

[84] J. D. Murray, *Mathematical Biology II: Spatial Models and Biomedical Applications*, edited by J. D. Murray (Springer, New York, 2003), Vol. 18.

[85] R. Colin, B. Ni, L. Laganenka, and V. Sourjik, Multiple functions of flagellar motility and chemotaxis in bacterial physiology, FEMS Microbiol. Rev. **45**, fuab038 (2021).

[86] J. Adler, Chemotaxis in bacteria, Science **153**, 708 (1966).

[87] P. H. Colberg and R. Kapral, Many-body dynamics of chemically propelled nanomotors, J. Chem. Phys. **147**, 064910 (2017).

[88] S. Mahdisoltani, R. B. A. Zinati, C. Duclut, A. Gambassi, and R. Golestanian, Nonequilibrium polarity-induced chemotaxis: Emergent Galilean symmetry and exact scaling exponents, Phys. Rev. Res. **3**, 013100 (2021).

[89] S. C. Takatori, W. Yan, and J. F. Brady, Swim Pressure: Stress Generation in Active Matter, Phys. Rev. Lett. **113**, 028103 (2014).

[90] V. M. Worlitzer, G. Ariel, A. Be'er, H. Stark, M. Bär, and S. Heidenreich, Motility-induced clustering and mesoscale turbulence in active polar fluids, New J. Phys. **23**, 033012 (2021).

[91] E. O. Budrene and H. C. Berg, Complex patterns formed by motile cells of escherichia coli, Nature (London) **349**, 630 (1991).

[92] S. Michelin, E. Lauga, and D. Bartolo, Spontaneous autophoretic motion of isotropic particles, Phys. Fluids **25**, 061701 (2013).

[93] S. Michelin and E. Lauga, Phoretic self-propulsion at finite péclet numbers, J. Fluid Mech. **747**, 572 (2014).

[94] We note, however, that below the S/O boundary shown by the dashed curve in Figs. 1(e) and 1(f), the simulations still show some initial nonstationary behavior—reflecting the limitation of our linear stability analysis, which is strictly only applicable to conditions close to the initial homogeneous state.

[95] P. Roca-Cusachs, R. Sunyer, and X. Trepat, Mechanical guidance of cell migration: Lessons from chemotaxis, Curr. Opin. Cell Biol. **25**, 543 (2013).

[96] A. Shellard and R. Mayor, All roads lead to directional cell migration, Trends Cell Biol. **30**, 852 (2020).

[97] S. SenGupta, C. A. Parent, and J. E. Bear, The principles of directed cell migration, Nat. Rev. Mol. Cell Biol. **22**, 529 (2021).

[98] R. Sunyer, V. Conte, J. Escribano, A. Elosegui-Artola, A. Labernadie, L. Valon, D. Navajas, J. M. García-Aznar, J. J. Muñoz, P. Roca-Cusachs, and X. Trepat, Collective cell durotaxis emerges from long-range intercellular force transmission, Science **353**, 1157 (2016).

[99] R. Alert and J. Casademunt, Role of substrate stiffness in tissue spreading: Wetting transition and tissue durotaxis, Langmuir **35**, 7571 (2019).

[100] D. J. Cohen, W. J. Nelson, and M. M. Maharbiz, Galvanotactic control of collective cell migration in epithelial monolayers, Nat. Mater. **13**, 409 (2014).

[101] M. Mijalkov, A. McDaniel, J. Wehr, and G. Volpe, Engineering Sensorial Delay to Control Phototaxis and Emergent Collective Behaviors, Phys. Rev. X **6**, 011008 (2016).

Chemotactic Motility Induced Phase Separation: Supplementary Information

Hongbo Zhao,[1] Andrej Košmrlj,[2, 3] and Sujit S. Datta[1]

[1] *Department of Chemical and Biological Engineering,*
Princeton University, Princeton, NJ 08544
[2] *Department of Mechanical and Aerospace Engineering,*
Princeton University, Princeton, NJ 08544
[3] *Princeton Materials Institute,*
Princeton University, Princeton, NJ 08544

S1. THERMODYNAMICS OF NON-CHEMOTACTIC ABPS

As derived in [1], the non-dimensional active pressure generated by ABPs in 2D is

$$\frac{\Pi}{n\zeta U_0^2 \tau_R/2} = 1 - \phi - 0.2\phi^2 + \frac{4}{\pi}\phi \mathrm{Pe}_R \left(1 - \frac{\phi}{\phi_m}\right)^{-1}, \quad (S1)$$

where n is the particle number density, ϕ is the area fraction $\phi = nv_0$, where $v_0 = \pi a^2$ is the area taken up by each particle, and $\phi_m = 0.9$ is the maximum area fraction ($0 \le \phi < \phi_m$). This pressure is also related to a nonequilibrium Helmholtz free energy per volume f,

$$\Pi = \phi^2 \frac{\partial}{\partial \phi}\left(\frac{f}{\phi}\right) = f'\phi - f. \quad (S2)$$

Combining Eqs. (S1)- (S2) then yields

$$\frac{f}{\zeta U_0^2 \tau_R/2} = \frac{\phi}{v_0}\left[\ln\phi - \phi - 0.1\phi^2 \right.$$
$$\left. - \frac{4}{\pi}\mathrm{Pe}_R \cdot \phi_m \ln\left(1 - \frac{\phi}{\phi_m}\right)\right]. \quad (S3)$$

Given this Helmholtz free energy, one can further define the bulk chemical potential, which we use in the calculations described in the main text: $\mu_h \equiv \partial f/\partial n = \partial(v_0 f)/\partial\phi$. As explained in the main text, we define a nondimensionalized version of it as $\tilde\mu_h \equiv \mu_h/(\zeta U_0^2 \tau_R/2)$. This definition yields

$$\tilde\mu_h = \ln\phi + 1 - 2\phi - 0.3\phi^2$$
$$- \frac{4}{\pi}\mathrm{Pe}_R \cdot \phi_m\left[\ln\left(1 - \frac{\phi}{\phi_m}\right) - \frac{\phi}{\phi_m - \phi}\right]. \quad (S4)$$

When analyzing the linear stability in § S3, we often need to evaluate the derivative of the non-dimensional chemical potential with respect to ϕ,

$$\partial_\phi \tilde\mu_h = \frac{1}{\phi} - 2 - 0.6\phi - \frac{4}{\pi}\mathrm{Pe}_R \cdot \frac{\phi_m(\phi - 2\phi_m)}{(\phi - \phi_m)^2}. \quad (S5)$$

It is useful to note that $-\partial_\phi \tilde\mu_h$ has an upper bound:

$$\sup_{\phi, \mathrm{Pe}_R}(-\partial_\phi \tilde\mu_h) = \lim_{\phi \to \phi_m, \mathrm{Pe}_R \to 0}-\partial_\phi\tilde\mu_h,$$

$$\sup_{\phi, \mathrm{Pe}_R}(-\partial_\phi \tilde\mu_h) = -\frac{1}{\phi_m} + 2 + 0.6\phi_m \approx 1.43. \quad (S6)$$

Consistent with the classical Cahn-Hilliard theory of phase separation, the free energy can be extended to penalize a sharp interface [2, 3]. The total free energy in a spatial field is

$$F = \int \left(f + \frac{1}{2}\frac{\zeta U_0^2 \tau_R}{2v_0}\kappa\|\nabla\phi\|^2\right)d\boldsymbol{x}, \quad (S7)$$

from which the overall chemical potential can be defined variationally by $\mu \equiv \delta F/\delta n = v_0 \delta F/\delta\phi$; here, $\kappa = l_0^2$ as noted in the main text. Again, we define a normalized version of this overall chemical potential $\tilde\mu \equiv \mu/(\zeta U_0^2 \tau_R/2)$. Therefore,

$$\tilde\mu = \tilde\mu_h - \kappa\nabla^2\phi, \quad (S8)$$

Using these thermodynamic rules, we next describe the phase dynamics following Ref. [1]. The particle volume fraction satisfies the conservation equation:

$$\frac{\partial\phi}{\partial t} = \nabla\cdot\left(\frac{\phi}{\zeta}\nabla\mu\right) = \nabla\cdot\left(M_0\phi\nabla\big(\tilde\mu_h(\phi, \mathrm{Pe}_R) - \tilde\kappa\nabla^2\phi\big)\right), \quad (S9)$$

where $M_0 = U_0^2 \tau_R/2$. For convenience of notation, we define the collective diffusivity $M(\phi) \equiv M_0\phi$. This expression thereby yields the part of Eq. (1) of the main text that reflects active Brownian motion.

S2. DERIVATION OF THE CONTINUUM MODEL OF CHEMOTAXIS

We introduce a modified model of self-phoretic active colloids that self-propel and chemotax in response to a chemical gradient based on Refs. [4, 5] where we take into account the inter-particle force,

$$\frac{d\boldsymbol{r}_i}{dt} = U_0\boldsymbol{e}_i + \frac{D_{\mathrm{tr}}}{k_B T}\boldsymbol{F}_i - \zeta_{\mathrm{tr}}\nabla\tilde c + \boldsymbol{\xi}_{\mathrm{tr},i}, \quad (S10)$$

$$\frac{d\boldsymbol{e}_i}{dt} = -\zeta_{\mathrm{rot}}(\boldsymbol{I} - \boldsymbol{e}_i \otimes \boldsymbol{e}_i)\nabla\tilde c + \boldsymbol{\xi}_{\mathrm{rot},i} \times \boldsymbol{e}_i, \quad (S11)$$

where $\boldsymbol{r}_i$ is the position of particle i, $\boldsymbol{e}_i$ is the orientation of particle i, D_{tr} is the translation diffusivity, $\boldsymbol{F}_i$ is the conservative inter-particle repulsive force on particle i, ζ_{tr} and ζ_{rot} are the translational and rotational diffusiophoretic coefficient, respectively, $\boldsymbol{I}$ is the identity tensor, $\boldsymbol{\xi}_{\mathrm{tr},i}$ and $\boldsymbol{\xi}_{\mathrm{rot},i}$ are the independent translation and rotational thermal noise and their time correlations satisfy $\langle\boldsymbol{\xi}_{\mathrm{tr},i}(t)\boldsymbol{\xi}_{\mathrm{tr},i}(t')\rangle = 2D_{\mathrm{tr}}\boldsymbol{I}\delta(t - t')$ and

$\langle \boldsymbol{\xi}_{\text{rot},i}(t)\boldsymbol{\xi}_{\text{rot},i}(t')\rangle = 2D_{\text{rot}}\boldsymbol{I}\delta(t - t')$, respectively, where $D_{\text{rot}} = 1/\tau_R$ is the rotational diffusivity.

In order to obtain a closed-form continuum model of chemotactic MIPS based on the microscopic model, we must make certain assumptions and use closures. We follow and adapt the established methods used to derive continuum equations for MIPS based on the ABP model and for chemotactic colloids. Specifically, in Ref. [4]'s derivation of a continuum model based on Eq. (S10) and (S11), a Smoluchowski equation for a single particle is used without considering the interaction between particles, and the Keller-Segel model is obtained as the lowest order equation for the particle density. We extend the derivation to the MIPS regime where particle-to-particle repulsion in the densely packed region needs to be considered to account for particle slowing-down in the dense region and hence is the key to modeling MIPS. To achieve this goal, we follow the derivation in Ref. [2, 6] based on a Smoluchowski equation for the probability distribution $\psi(\boldsymbol{r}, \boldsymbol{e}, t)$ of finding a single particle at position $\boldsymbol{r}$ moving in direction $\boldsymbol{e}$ and add the additional phoretic terms in Eq. (S10) and (S11) that involves ζ_{tr} and ζ_{rot} to obtain

$$\frac{\partial\psi}{\partial t} = -\nabla\cdot(\psi v\boldsymbol{e}) + \nabla\cdot(D_{\text{tr}}\nabla\psi) + \zeta_{\text{tr}}\nabla\cdot(\psi\nabla\tilde{c})$$
$$+ \zeta_{\text{rot}}\partial_\varphi(\psi\partial_\varphi\boldsymbol{e}\cdot\nabla\tilde{c}) + D_{\text{rot}}\partial_\varphi^2\psi, \quad \text{(S12)}$$

where we consider the 2D case for simplicity, and φ is the orientation angle that corresponds to $\boldsymbol{e}$, v is the self-propulsion speed that is assumed to be isotropic (no dependence on $\boldsymbol{e}$) and depends on local particle density [2, 6, 7]. Particle density is defined to be

$$n(\boldsymbol{r},t) = \int \psi(\boldsymbol{r},\varphi,t)d\varphi. \quad \text{(S13)}$$

Additionally, we define polar order

$$\boldsymbol{p}(\boldsymbol{r},t) = \int \psi(\boldsymbol{r},\varphi,t)\boldsymbol{e}d\varphi, \quad \text{(S14)}$$

nematic order tensor

$$\boldsymbol{Q}(\boldsymbol{r},t) = \int \psi(\boldsymbol{r},\varphi,t)\left(\boldsymbol{e}\otimes\boldsymbol{e} - \frac{1}{2}\right)d\varphi, \quad \text{(S15)}$$

and the third order harmonics $\boldsymbol{P}_3$ defined by (following Ref. [4]'s notation)

$$\boldsymbol{P}_3(\boldsymbol{r},t) = \int \psi(\boldsymbol{r},\varphi,t)\left(\boldsymbol{e}\otimes\boldsymbol{e}\otimes\boldsymbol{e} - \frac{3}{4}\boldsymbol{e}\mathbb{1}\right)d\varphi, \quad \text{(S16)}$$

where $(\boldsymbol{e}\mathbb{1})_{ijk} = (e_i\delta_{jk} + e_j\delta_{ik} + e_k\delta_{ij})/3$. Following Ref. [4] and integrating Eq. (S12), we obtain the dynamical equation for particle density

$$\frac{\partial n}{\partial t} = -\nabla\cdot(v\boldsymbol{p}) + \nabla\cdot(D_{\text{tr}}\nabla n) + \zeta_{\text{tr}}\nabla\cdot(n\nabla\tilde{c}). \quad \text{(S17)}$$

Integrating Eq. (S12) multiplied by $\boldsymbol{e}$, we obtain the dynamical equation for polar order

$$\frac{\partial\boldsymbol{p}}{\partial t} = -\nabla\cdot(v\boldsymbol{Q}) - \frac{1}{2}\nabla(vn) + \nabla\cdot(D_{\text{tr}}\nabla\boldsymbol{p})$$
$$+ \zeta_{\text{tr}}\nabla\cdot(\boldsymbol{p}\otimes\nabla\tilde{c}) + \zeta_{\text{rot}}\left(\boldsymbol{Q} - \frac{1}{2}n\boldsymbol{I}\right)\nabla\tilde{c} - D_{\text{rot}}\boldsymbol{p}.$$
$$\text{(S18)}$$

Following Ref. [2, 4], the dynamical equation for nematic order is

$$\frac{\partial\boldsymbol{Q}}{\partial t} = -\frac{1}{4}\left(\nabla(v\boldsymbol{p}) + [\nabla(v\boldsymbol{p})]^T - \nabla\cdot(v\boldsymbol{p})\boldsymbol{I}\right) - \nabla\cdot(v\boldsymbol{P_3})$$
$$+ \nabla\cdot(D_{\text{tr}}\nabla\boldsymbol{Q}) + \zeta_{\text{tr}}\nabla\cdot(\boldsymbol{Q}\otimes\nabla\tilde{c})$$
$$+ \zeta_{\text{rot}}\left(2\boldsymbol{P}_3 - \frac{3}{2}\boldsymbol{p}\mathbb{1} + \boldsymbol{I}\otimes\boldsymbol{p}\right)\nabla\tilde{c} - 4D_{\text{rot}}\boldsymbol{Q}, \quad \text{(S19)}$$

where similar to $\boldsymbol{e}\mathbb{1}$, $\boldsymbol{p}\mathbb{1} = (p_i\delta_{jk} + p_j\delta_{ik} + p_k\delta_{ij})/3$. For clarity, we express the last term in index notation $\zeta_{\text{rot}}\left(2\boldsymbol{P}_{3,ijk} + \frac{1}{2}p_i\delta_{jk} - \frac{1}{2}p_j\delta_{ik} - \frac{1}{2}p_k\delta_{ij}\right)\partial_i\tilde{c}$. Following Ref. [2, 4, 6], at a time scale much larger than the reorientation time τ_R and length scale much larger than the persistence length l_0, the high order moments $\boldsymbol{p}$ and $\boldsymbol{Q}$ reach steady state much faster than n. From $\frac{\partial\boldsymbol{Q}}{\partial t} \approx 0$, we get the nematic order tensor

$$\boldsymbol{Q} = \frac{1}{4D_{\text{rot}}}\left(-\frac{1}{4}\left(\nabla(v\boldsymbol{p}) + [\nabla(v\boldsymbol{p})]^T - \nabla\cdot(v\boldsymbol{p})\boldsymbol{I}\right)\right.$$
$$\left. - \nabla\cdot(v\boldsymbol{P_3}) + \zeta_{\text{rot}}\left(2\boldsymbol{P}_3 - \frac{3}{2}\boldsymbol{p}\mathbb{1} + \boldsymbol{I}\otimes\boldsymbol{p}\right)\nabla\tilde{c}\right)$$
$$+ O(\nabla^2), \quad \text{(S20)}$$

where $O(\nabla^2)$ refers to all terms involving second or higher mixed order derivatives of $\boldsymbol{p}$, $\boldsymbol{P}_3$, and $\tilde{c}$. Substituting into $\frac{\partial\boldsymbol{p}}{\partial t} \approx 0$, we get the polar order

$$\boldsymbol{p} = -\frac{1}{2D_{\text{rot}}}\left(\nabla(vn) + \zeta_{\text{rot}}n\nabla\tilde{c}\right) + O(\nabla^2), \quad \text{(S21)}$$

where $O(\nabla^2)$ refers to all terms involving second or higher mixed order derivatives of n, $\boldsymbol{P}_3$ and $\tilde{c}$. Substituting into Eq. (S17), we get the evolution of the particle density

$$\frac{\partial n}{\partial t} = -\nabla\cdot(\boldsymbol{V}n - D\nabla n + \chi n\nabla\tilde{c}) + o(\nabla^2), \quad \text{(S22)}$$

where

$$\boldsymbol{V} = -\frac{v\nabla v}{2D_{\text{rot}}}, \quad \text{(S23)}$$

$$D = \frac{v^2}{2D_{\text{rot}}} + D_{\text{tr}}, \quad \text{(S24)}$$

$$\chi = -\left(\frac{\zeta_{\text{rot}}v}{2D_{\text{rot}}} + \zeta_{\text{tr}}\right) \quad \text{(S25)}$$

and $o(\nabla^2)$ refers to all terms involving mixed derivatives of n and $\tilde{c}$ of order higher than 2. Following Ref. [2], v,

D_{rot}, and D_{tr} depend on local particle density n, hence $\boldsymbol{V}$, D, and χ are functions (or in general functionals) of n, and we define excess free energy functional $F_{\text{ex}}[n]$ such that

$$-\frac{\boldsymbol{V}}{D} = \nabla\left(\frac{\delta F_{\text{ex}}}{\delta n}\right) \tag{S26}$$

and define the free energy function $F[n] = F_{\text{ex}}[n] + \int n(\ln n - 1)d\boldsymbol{x}$, and substituting into Eq. (S22) we obtain the following closed dynamical equation for n up to diffusion and convection terms,

$$\frac{\partial n}{\partial t} = \nabla \cdot \left(Dn\nabla\left(\frac{\delta F}{\delta n}\right) - \chi n\nabla\tilde{c}\right). \tag{S27}$$

It is known that the local speed v decreases with increasing particle density due to crowding [7]. This can lead to a concave free energy near the onset of instability and hence MIPS. To obtain the leading order model, we consider χ to be a constant ($\chi \approx \chi_0$, which occurs in the limit of $\zeta_{\text{tr}} \gg \zeta_{\text{rot}}U_0/(2D_{\text{rot}})$). Similarly, we approximate the diffusivity D to be a constant, and when the diffusivity is due to randomly-oriented self-propulsion, $D \sim U_0^2\tau_R$. Finally, by converting the number density n to volume fraction ϕ and using the free energy model described in §S1, we arrive at the leading order model for chemotactic MIPS (Eqs. (1-2) in the main text)

$$\frac{\partial\phi}{\partial t} = \nabla \cdot (M_0\phi\nabla(\tilde{\mu}_h(\phi, \text{Pe}_R) - \kappa\nabla^2\phi) - \chi_0\phi\nabla\tilde{c}). \tag{S28}$$

In the derivation above going from Eq. (S22) to Eq. (S27), we made the assumption that the self-propulsion speed of a single freely-moving particle (U_0) is constant and independent of the chemical concentration $\tilde{c}$, and hence v, D_{rot}, and D_{tr} are also independent of $\tilde{c}$ and only depend on n. For simplicity, the work presented here and in the main text focuses on this case in which the self-propulsion velocity is independent of $\tilde{c}$; however, in some cases, the self-propulsion speed can depend on the chemical concentration. In this case, the general derivation spanning Eqs. (S12) to (S22) still holds; that is, Eq. (S22) remains true when v, D_{rot}, D_{tr}, ζ_{rot}, and ζ_{tr} are also functions of both n and $\tilde{c}$, since no constraints are imposed on these variables. In this case, $\boldsymbol{V}$, D, and χ depend on both n and $\tilde{c}$. In general, the "integrability" condition [Eq. (S26)] may not be satisfied. However, when the translational diffusivity of particles due to thermal noise D_{tr} is negligible compared to the active part $v^2/(2D_{\text{rot}})$, which is often the case as discussed in Ref. [7], $-\boldsymbol{V}/D = \nabla\ln v[n,\tilde{c}]$. This relation always satisfies the integrability condition [7, 8] and $\frac{\delta F_{\text{ex}}}{\delta n} = \ln v[n,\tilde{c}]$. Therefore, Eq. (S27) still holds and we arrive at a generalized version of Eq. (S28) where the chemical potential $\tilde{\mu}_h(\phi,\tilde{c})$ can depend on $\tilde{c}$,

$$\frac{\partial\phi}{\partial t} = \nabla \cdot (M_0\phi\nabla(\tilde{\mu}_h(\phi,\tilde{c}) - \kappa\nabla^2\phi) - \chi_0\phi\nabla\tilde{c}). \tag{S29}$$

This equation introduces a new coupling between ϕ and $\tilde{c}$ and therefore a new way that the chemical concentration

can affect the phase separation. The specific form of $\tilde{\mu}_h$ is then determined by the exact functional dependence of self-propulsion speed v on n and $\tilde{c}$.

S3. LINEAR STABILITY ANALYSIS

A. Dispersion relation

In this section, we study the linear stability of the governing equations, Eqs. (1)-(3) of the main text. For generality, here we do not assume any particular functional form for the chemotactic sensing function $f(\tilde{c})$ or chemoattractant uptake rate $g(\tilde{c})$. We perturb the homogeneous steady state $\phi(\boldsymbol{x}) = \phi_0$ and $\tilde{c}(\boldsymbol{x}) = \tilde{c}_0 = g^{-1}(Sk^{-1}\phi_0^{-1})$ with small amplitude perturbations $\delta\phi = \delta\hat{\phi}e^{i\boldsymbol{q}\cdot\boldsymbol{x}+\omega t}$, and $\delta\tilde{c} = \delta\hat{c}e^{i\boldsymbol{q}\cdot\boldsymbol{x}+\omega t}$. Linearizing Eqs. (1)-(3) and substituting $\delta\phi$ and $\delta\tilde{c}$ yields

$$\omega\delta\hat{\phi} = -M(\phi_0)q^2(\partial_\phi\tilde{\mu}_h(\phi_0) + \kappa q^2)\delta\hat{\phi} + \chi_0\phi_0 q^2 f'(\tilde{c}_0)\delta\hat{c}, \tag{S30}$$

$$\omega\delta\hat{c} = -D_c q^2\delta\hat{c} - k(g(\tilde{c}_0)\delta\hat{\phi} + \phi_0 g'(\tilde{c}_0)\delta\hat{c}), \tag{S31}$$

where $q = |\boldsymbol{q}|$. For simplicity of notation, in the following text, the arguments ϕ_0 and $\tilde{c}_0$ in $\partial_\phi\tilde{\mu}_h(\phi_0)$, $g(\tilde{c}_0)$, $g'(\tilde{c}_0)$, and $f'(\tilde{c}_0)$ are omitted. The eigenvalue ω satisfies

$$\omega^2 + (\mathcal{M} + \mathcal{D})\omega + \mathcal{M}\mathcal{D} + \mathcal{X} = 0. \tag{S32}$$

The solution to ω is

$$\omega_\pm = \frac{1}{2}\left(-(\mathcal{M} + \mathcal{D}) \pm \sqrt{(\mathcal{M} - \mathcal{D})^2 - 4\mathcal{X}}\right), \tag{S33}$$

where

$$\begin{aligned}\mathcal{M} &\equiv Mq^2(\partial_\phi\tilde{\mu}_h + \kappa q^2), \\ \mathcal{D} &\equiv D_c q^2 + k\phi_0 g', \\ \mathcal{X} &\equiv k\chi_0\phi_0 f'gq^2.\end{aligned} \tag{S34}$$

In conventional non-chemotactic MIPS ($\chi_0 = 0$), the two eigenvalues are $-\mathcal{M}$ and $-\mathcal{D}$, respectively. Because $\mathcal{D} \geq 0$, the stability is determined by $\mathcal{M}$. When $\partial_\phi\tilde{\mu}_h < 0$, or in the spinodal region as defined in the main text, ω can be positive in a range of wavenumber q, and the most unstable wavenumber that corresponds to maximum instability growth rate ω is $q_{\text{sp}}^{-1} \equiv \sqrt{-2\kappa/\partial_\phi\tilde{\mu}_h}$. Because of Eq. (S6), $q_{\text{sp}}^{-1} \gtrsim l_0$. In the majority of this section and the manuscript, we focus on the MIPS spinodal region. We provide a discussion of linear stability analysis outside the spinodal region in §S3 E. By nondimensionalizing wavenumber with the characteristic length scale of spinodal decomposition,

$$\tilde{q} \equiv \sqrt{-\frac{\kappa}{\partial_\phi\tilde{\mu}_h}}q = \frac{q}{\sqrt{2}q_{\text{sp}}}, \tag{S35}$$

and nondimensionalizing rate with the characteristic growth rate of non-chemotactic spinodal decomposition $4\omega_{\text{sp}} = 4\omega(q_{\text{sp}}, \text{Pe}_C = 0) = M(\partial_\phi\tilde{\mu}_h)^2/\kappa$, $\tilde{\omega} \equiv$

$\omega/(4\omega_{\rm sp})$, $\tilde{\mathcal{M}} \equiv \mathcal{M}/(4\omega_{\rm sp})$, $\tilde{\mathcal{D}} \equiv \mathcal{D}/(4\omega_{\rm sp})$, $\tilde{\mathcal{X}} \equiv \mathcal{X}/(4\omega_{\rm sp})^2$, we obtain the nondimensionalized equation for the eigenvalues

$$\tilde{\omega}^2 + (\tilde{\mathcal{M}} + \tilde{\mathcal{D}})\tilde{\omega} + \tilde{\mathcal{M}}\tilde{\mathcal{D}} + \tilde{\mathcal{X}} = 0. \qquad (S36)$$

The solution is then

$$\tilde{\omega}_{\pm} = \frac{1}{2}\left(-(\tilde{\mathcal{M}} + \tilde{\mathcal{D}}) \pm \sqrt{(\tilde{\mathcal{M}} - \tilde{\mathcal{D}})^2 - 4\tilde{\mathcal{X}}}\right), \quad (S37)$$

where

$$\tilde{\mathcal{M}} = \tilde{q}^2\left(-1 + \tilde{q}^2\right),$$
$$\tilde{\mathcal{D}} = \frac{1}{\alpha}\left(\tilde{q}^2 + {\rm Da}\right), \qquad (S38)$$
$$\tilde{\mathcal{X}} = \frac{\rm Da}{\alpha}{\rm Pe}'_C\tilde{q}^2,$$

and the dimensionless parameters are

$$\alpha = -\frac{M\partial_\phi\tilde{\mu}_h}{D_c},$$
$${\rm Da} = -\frac{\kappa k\phi_0 g'}{D_c\partial_\phi\tilde{\mu}_h}, \qquad (S39)$$
$${\rm Pe}'_C = -\frac{\chi_0}{M\partial_\phi\tilde{\mu}_h}\frac{f'g}{g'}.$$

We restrict our discussion below to $\partial_\phi\tilde{\mu}_h < 0$ (in the spinodal region), $\alpha > 0$, ${\rm Da} > 0$, and ${\rm Pe}'_C \geq 0$.

B. Stability condition

When the discriminant of the quadratic equation Eq. (S36) is positive, i.e., $\Delta \equiv (\tilde{\mathcal{M}} - \tilde{\mathcal{D}})^2 - 4\tilde{\mathcal{X}} > 0$, it can be seen from Eq. (S37) that $\tilde{\omega}_+$ decreases with increasing ${\rm Pe}'_C$. In other words, chemotaxis has a stabilizing effect. Therefore, next, we derive the condition under which the system is stable, that is, ${\rm Re}\,\tilde{\omega}_{\pm}(\tilde{q}) \leq 0$ for all $\tilde{q}$. This condition is equivalent to (1) $I_2 \equiv \tilde{\omega}_+\tilde{\omega}_- = \tilde{\mathcal{M}}\tilde{\mathcal{D}} + \tilde{\mathcal{X}} \geq 0$, and (2) $I_1 \equiv \tilde{\omega}_+ + \tilde{\omega}_- = -(\tilde{\mathcal{M}} + \tilde{\mathcal{D}}) \leq 0$ for all $\tilde{q}$.

Criterion (1) ($I_2 \geq 0$) can be achieved with sufficiently large ${\rm Pe}'_C$: since

$$I_2 = \frac{\tilde{q}^2}{\alpha}\left((\tilde{q}^2 - 1)(\tilde{q}^2 + {\rm Da}) + {\rm Da}{\rm Pe}'_C\right), \qquad (S40)$$

$I_2 \geq 0$ for all $\tilde{q}$ is equivalent to $\min_{\tilde{q}}\alpha\tilde{q}^{-2}I_2 \geq 0$. When ${\rm Da} \leq 1$, the minimum is obtained at $\tilde{q} = 0$, and $\min_{\tilde{q}}\alpha\tilde{q}^{-2}I_2 = {\rm Da}({\rm Pe}'_C - 1)$; hence, criterion (1) is equivalent to ${\rm Pe}'_C > 1$. When ${\rm Da} > 1$, the minimum is obtained at $\tilde{q}^2 = (1 - {\rm Da})/2$, and

$$\min_{\tilde{q}}\alpha\tilde{q}^{-2}I_2 = -\frac{(1 + {\rm Da})^2}{4} + {\rm Da}{\rm Pe}'_C. \qquad (S41)$$

In this case criterion (1) is equivalent to ${\rm Pe}'_C > (1 + {\rm Da})^2/(4{\rm Da})$. Therefore, we can summarize criterion (1) in a more compact form as

$${\rm Pe}'_C > {\rm Pe}'_{C{\rm crit}} = \frac{(1 + \min\{{\rm Da}, 1\})^2}{4\min\{{\rm Da}, 1\}}. \qquad (S42)$$

In other words, in order to suppress phase separation, chemotactic rate needs to be sufficiently fast.

As noted above, at the critical point of stability where $\max_{\tilde{q}} I_2 = 0$, the critical wavenumber is

$$\tilde{q}_{\rm crit,2}^2 = \frac{1 - \min\{{\rm Da}, 1\}}{2}. \qquad (S43)$$

This result indicates that if criterion (2) is satisfied so that the stability of the system is solely determined by criterion (1), as the control parameter ${\rm Pe}'_C$ varies near the critical condition of stability, the range of unstable wavelength can either be unbounded ($\tilde{q}$ near 0) if ${\rm Da} \geq 1$ or finite ($\tilde{q}$ near $\sqrt{(1 - {\rm Da})/2}$) if ${\rm Da} \leq 1$. The former belongs to type F instability while the latter belongs to type U instability according to Cross and Hohenberg's classification of dispersion relations [9].

Having large ${\rm Pe}'_C$ is a necessary but insufficient condition for the suppression of phase separation. Another way to interpret criterion (2) ($I_1 \leq 0$) is that, when ${\rm Pe}'_C$ is sufficiently large, Δ becomes negative, and ${\rm Re}\,\tilde{\omega}_{\pm} = -(\tilde{\mathcal{M}} + \tilde{\mathcal{D}})/2 = I_1/2$. Hence, sufficiently large ${\rm Pe}'_C$ can fully stabilize the system only when $I_1 < 0$.

Since

$$I_1 = -\tilde{q}^4 + \left(1 - \frac{1}{\alpha}\right)\tilde{q}^2 - \frac{\rm Da}{\alpha}, \qquad (S44)$$

when $\alpha \leq 1$, the maximum is obtained at $\tilde{q} = 0$, and $\max_{\tilde{q}} I_1 = -{\rm Da}/\alpha < 0$. When $\alpha > 1$, the maximum is obtained at $\tilde{q}^2 = (\alpha - 1)/2\alpha$, and

$$\max_{\tilde{q}} I_1 = \frac{1}{\alpha}\left(\frac{(\alpha - 1)^2}{4\alpha} - {\rm Da}\right). \qquad (S45)$$

$I_1 \leq 0$ for all $\tilde{q}$ is equivalent to $\max_{\tilde{q}} I_1 < 0$, or equivalently $\alpha \leq 1$ or ${\rm Da} \geq (\alpha - 1)^2/4\alpha$. This condition can be written in a more compact form as shown in the main text,

$$\alpha \leq \alpha_{\rm crit} = 1 + 2 \cdot {\rm Da} + 2\sqrt{{\rm Da}(1 + {\rm Da})}. \qquad (S46)$$

Or alternatively,

$${\rm Da} \geq {\rm Da}_{\rm crit} = \frac{(1 - \max\{\alpha, 1\})^2}{4\max\{\alpha, 1\}}. \qquad (S47)$$

In other words, in order to suppress phase separation, chemoattractant diffusion or uptake rate needs to be sufficiently fast.

As noted above, at the critical condition of stability where $\max_{\tilde{q}} I_1 = 0$, the critical wavenumber is

$$\tilde{q}_{\rm crit,1}^2 = \frac{1 - \alpha^{-1}}{2}. \qquad (S48)$$

This result indicates that if criterion (1) is satisfied so that the stability of the system is solely determined by criterion (2), as the control parameter α or ${\rm Da}$ varies near the critical condition of stability, the range of unstable

mode is finite and near $\tilde{q}_{\mathrm{crit},1}$. This belongs to type F instability according to Cross and Hohenberg's classification of dispersion relations [9].

In summary, the stability criteria (1) and (2) are equivalent to $\mathrm{Pe}'_C \geq \mathrm{Pe}'_{C\mathrm{crit}}$ and $\alpha \leq \alpha_{\mathrm{crit}}$ (or $\mathrm{Da} \geq \mathrm{Da}_{\mathrm{crit}}$), indicating that MIPS can be suppressed with sufficiently fast chemotaxis and chemoattractant diffusion (or uptake rate).

C. Finite and unbounded wavelength instabilities

In the main text, we define finite and unbounded wavelength instabilities based on the range of unstable modes, which we here express in dimensionless form: $\tilde{q}_{u-} < \tilde{q} < \tilde{q}_{u+}$. When $\tilde{q}_{u-} = 0$, the unstable wavelength extends all the way to infinity—we thus call this an unbounded instability (type U). Otherwise when $\tilde{q}_{u-} > 0$, the range of unstable wavelengths is finite—we thus call this a finite wavelength instability (type F).

From Eq. (S37), we see that $\tilde{\omega}_+(\tilde{q} = 0) = 0$ and $\tilde{\omega}'_+(\tilde{q} = 0) = 0$. Hence the sign of the second order derivative determines whether modes near $\tilde{q} = 0$ are stable. At $\tilde{q} = 0$,

$$\tilde{\omega}''_+ = - \frac{(\tilde{\mathcal{M}}\tilde{\mathcal{D}} + \tilde{\mathcal{X}})''}{\tilde{\mathcal{M}} + \tilde{\mathcal{D}}}\bigg|_{\tilde{q}=0} = 2(1 - \mathrm{Pe}'_C). \qquad (S49)$$

When $\mathrm{Pe}'_C < 1$, $\tilde{\omega}''(\tilde{q} = 0) > 0$, we have $\tilde{q}_{u-} = 0$, hence the system has an unbounded instability. Otherwise, when $\mathrm{Pe}'_C > 1$ and the system is in the unstable regime, it has a finite wavelength instability. These results suggest that as the chemotactic rate increases, modes near zero wavenumber become stabilized—and thus, phase separated domains are less likely to coarsen since chemotaxis disperses the particles.

When criterion (2) described in § S3 B is satisfied, the dispersion relation can be classified by Pe'_C. If $\mathrm{Da} < 1$, the system has type U instability when $\mathrm{Pe}'_C < 1$, type F instability when $1 < \mathrm{Pe}'_C < \mathrm{Pe}'_{C\mathrm{crit}}$, and is stable when $\mathrm{Pe}'_C > \mathrm{Pe}'_{C\mathrm{crit}}$. The transition from instability to stability by increasing chemotactic rate is of type F [9]. Hence, when chemoattractant uptake rate is slow such that $\mathrm{Da} < 1$, finite-sized domains can be observed near the boundary of stability.

If $\mathrm{Da} > 1$, the system has type U instability when $\mathrm{Pe}'_C < 1$, and is stable when $\mathrm{Pe}'_C > 1$. The transition from instability to stability by increasing chemotactic rate is of type U [9]. Hence when chemoattractant uptake rate is fast such that $\mathrm{Da} > 1$, phase separated domains are more likely to coarsen near the boundary of stability.

The classification of type F/U instability also applies when criterion (2) is not satisfied, which we describe in the next section.
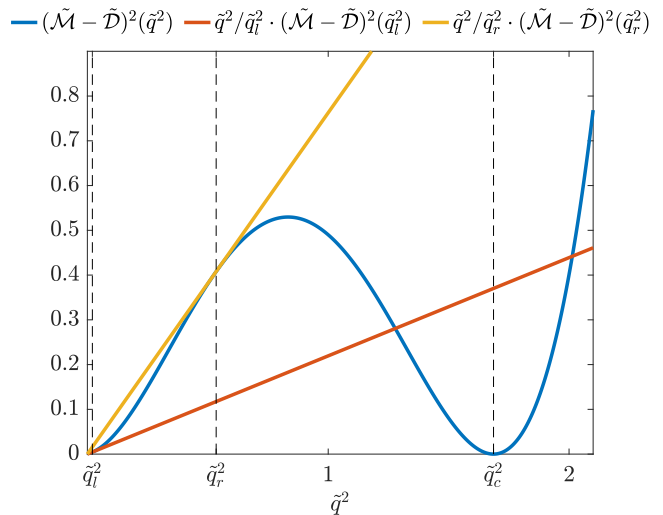

FIG. S1: A plot of $(\tilde{\mathcal{M}} - \tilde{\mathcal{D}})^2(\tilde{q}^2)$ and two lines that pass through the origin and are tangent to the curve at $\tilde{q}_l^2$ and $\tilde{q}_r^2$. $\mathrm{Da} = 0.05$, $\alpha = 1.5$.

D. Oscillatory instability condition

In § S3 B we have shown that when criterion (2) is not satisfied, large Pe'_C cannot suppress phase separation. Instead, at high enough Pe'_C, the discriminant becomes negative $\Delta < 0$, which means that eigenvalues can have imaginary part ($\mathrm{Im}\,\tilde{\omega} \neq 0$). Therefore, next, we derive the condition for oscillatory instability—that there exists $\tilde{q}$ for which $\mathrm{Re}\,\tilde{\omega} > 0$ and $\mathrm{Im}\,\tilde{\omega} \neq 0$, or equivalently $I_1 > 0$ and $\Delta < 0$.

Since I_1 is a quadratic polynomial of $\tilde{q}^2$, $I_1 > 0$ can be obtained by finding the values of $\tilde{q}^2$ that correspond to the zeros of I_1:

$$\tilde{q}_\pm^2 = \frac{\alpha - 1 \pm \sqrt{(\alpha - 1)^2 - 4\alpha\mathrm{Da}}}{2\alpha}. \qquad (S50)$$

In this section, we always require that $\alpha > 1$ and $\mathrm{Da} < (\alpha - 1)^2/4\alpha$ (criterion (2) is not satisfied). This ensures that $\tilde{q}_\pm^2$ exist and are positive. $I_1 > 0$ when $\tilde{q}_- < \tilde{q} < \tilde{q}_+$. Notice that $\tilde{q}_+ < (\alpha - 1)/\alpha < 1$.

Fig. S1 shows a typical plot of $(\tilde{\mathcal{M}} - \tilde{\mathcal{D}})^2$ as a function of $\tilde{q}^2$ in blue while $\tilde{\mathcal{X}}$ as a function of $\tilde{q}^2$ is a line that passes through the origin whose slope is proportional to Pe'_C. The intersection of these two curves is where $\Delta = 0$, and the region of $\Delta < 0$ is where $(\tilde{\mathcal{M}} - \tilde{\mathcal{D}})^2$ is below the line $\tilde{\mathcal{X}}$. When $\mathrm{Pe}'_C = 0$, $\Delta \geq 0$. As Pe'_C increases, the slope of $\tilde{\mathcal{X}}$ increases, the range of wavenumbers in which $\Delta < 0$ expands.

Because Δ is a quartic polynomial of $\tilde{q}^2$, it has at most four roots. Now we would like to analyze the properties of its roots in order to determine the region of $\Delta < 0$.

Notice that $\tilde{\mathcal{M}} - \tilde{\mathcal{D}}$ has one valid root,

$$\tilde{q}_c^2 = \frac{\alpha + 1 + \sqrt{(\alpha + 1)^2 + 4\alpha\mathrm{Da}}}{2\alpha}, \qquad (S51)$$

as shown in Fig. S1. Note that $\tilde{q}_c^2 > (\alpha + 1)/\alpha > 1$. Hence, when $\text{Pe}_C' > 0$, $(\tilde{\mathcal{M}} - \tilde{\mathcal{D}})^2$ and $\tilde{\mathcal{X}}$ has at least one intersection beyond $\tilde{q}_c^2$. This is shown graphically in Fig. S1, where we see that any straight line that goes through the origin has one interaction with the blue curve at $\tilde{q}^2 > \tilde{q}_c^2$. In other words, Δ has one root greater than $\tilde{q}_c^2$.

Since we are interested in the region $I_1 > 0$, or $\tilde{q}_- < \tilde{q} < \tilde{q}_+$, and we have $\tilde{q}_+ < 1 < \tilde{q}_c$, next, we focus on the roots of Δ within $[0, q_c]$. Because at $\tilde{q} = 0$, $(\tilde{\mathcal{M}} - \tilde{\mathcal{D}})^2 > 0$ and $\tilde{\mathcal{X}} = 0$, there is at least one root within $[0, q_c]$. Therefore, within this interval, there can be 1, 2, or 3 roots in total.

Having 2 roots in this interval or 3 roots in total for a quartic polynomial means that it has one root of multiplicity 2, or $\Delta = 0$ and $d\Delta/d\tilde{q}^2 = 0$. Graphically, this corresponds to the line $\tilde{\mathcal{X}}$ being tangent to $(\tilde{\mathcal{M}} - \tilde{\mathcal{D}})^2$, as shown in Fig. S1, where there are two solutions, and the root of multiplicity 2 is denoted as $\tilde{q}_l^2$ and $\tilde{q}_r^2$ respectively. Mathematically it is equivalent to:

$$\frac{(\tilde{\mathcal{M}} - \tilde{\mathcal{D}})^2}{\tilde{q}^2} = \frac{d\left((\tilde{\mathcal{M}} - \tilde{\mathcal{D}})^2\right)}{d\tilde{q}^2}, \tag{S52}$$

or

$$\frac{\tilde{\mathcal{M}} - \tilde{\mathcal{D}}}{\tilde{q}^2} = 2\frac{d(\tilde{\mathcal{M}} - \tilde{\mathcal{D}})}{d\tilde{q}^2}. \tag{S53}$$

Substituting in $\tilde{\mathcal{M}}$ and $\tilde{\mathcal{D}}$ [Eq. (S34)], we obtain

$$3\alpha q^4 - (1 + \alpha)q^2 + \text{Da} = 0. \tag{S54}$$

A solution exists when

$$\text{Da} \leq \frac{(\alpha + 1)^2}{12\alpha}, \tag{S55}$$

and the roots are

$$\tilde{q}_{l,r}^2 = \frac{\alpha + 1 \pm \sqrt{(\alpha + 1)^2 - 12\alpha\text{Da}}}{6\alpha}. \tag{S56}$$

In the above equation, $\tilde{q}_l^2$ takes the minus sign and $\tilde{q}_r^2$ takes the plus sign. In the discussion below, whenever we refer to $\tilde{q}_{l,r}$, we imply that the inequality in Eq. (S55) holds. The Péclet number Pe_C' that corresponds to the tangent lines $\Delta(\tilde{q}_{l,r}^2) = 0$ is

$$\text{Pe}_{C,l,r}' = \frac{(\tilde{\mathcal{M}} - \tilde{\mathcal{D}})^2(\tilde{q}_{l,r}^2)}{4\alpha^{-1}\text{Da}\tilde{q}_{l,r}^2} = \frac{(\alpha\tilde{q}_{l,r}^4 - (1 + \alpha)\tilde{q}_{l,r}^2 - \text{Da})^2}{4\alpha\text{Da}\tilde{q}_{l,r}^2}$$

$$\text{Pe}_{C,l,r}' = \frac{((\alpha + 1)\tilde{q}_{l,r}^2 + 2\text{Da})^2}{9\alpha\text{Da}\tilde{q}_{l,r}^2}. \tag{S57}$$

When $0 < \text{Pe}_C' < \text{Pe}_{C,l}'$, Δ has one root $\tilde{q}_1$ in $(\tilde{q}_r, \tilde{q}_c)$ and $\Delta < 0$ in $(q_1, q_c]$. When $\text{Pe}_{C,l} < \text{Pe}_C' < \text{Pe}_{C,r}$, Δ has three roots, $\tilde{q}_2 \in (0, \tilde{q}_l)$, $\tilde{q}_3 \in (\tilde{q}_l, \tilde{q}_r)$, and $\tilde{q}_4 \in (\tilde{q}_r, \tilde{q}_c)$, and $\Delta < 0$ in (q_2, q_3) and $(q_4, q_c]$. When $\text{Pe}_C' > \text{Pe}_{C,r}$, Δ has one root $\tilde{q}_5 \in [0, \tilde{q}_l]$, and $\Delta < 0$ in $(q_5, q_c]$. When

$\text{Da} > (\alpha + 1)^2/12\alpha$, $\tilde{q}_{l,r}$ does not exist and Δ has one root in $[0, \tilde{q}_c]$.

Recall that we are seeking the condition for unstable oscillatory modes, or $\Delta < 0$ within the interval of $[\tilde{q}_-, \tilde{q}_+]$. Since the interval in which $\Delta < 0$ expands with increasing Pe_C', we need to find the critical condition that there exists $\tilde{q}^* \in [\tilde{q}_-, \tilde{q}_+]$ for which $\Delta(\tilde{q}^*) = 0$ and for all $\tilde{q} \in [\tilde{q}_-, \tilde{q}_+]$, $\Delta(\tilde{q}) \geq 0$. Therefore it is important to determine the order of $\tilde{q}_\pm$ and $\tilde{q}_{l,r}$.

Setting $\tilde{q}_\pm = \tilde{q}_{l,r}$, we find that $\tilde{q}_-$ or $\tilde{q}_+$ is equal to $\tilde{q}_l$ or $\tilde{q}_r$ when

$$\text{Da} = 1 - \frac{2}{\alpha}. \tag{S58}$$

Furthermore, we find that when $\text{Da} < 1 - 2/\alpha$, $\tilde{q}_l < \tilde{q}_- < \tilde{q}_r < \tilde{q}_+$. When $\text{Da} > 1 - 2/\alpha$, the orders are: $\tilde{q}_l < \tilde{q}_- < \tilde{q}_+ < \tilde{q}_r$ when $1 < \alpha < 3$; $\tilde{q}_l < \tilde{q}_r < \tilde{q}_- < \tilde{q}_+$, when $3 < \alpha < 5$, and $\tilde{q}_- < \tilde{q}_l < \tilde{q}_r < \tilde{q}_+$ when $\alpha > 5$. Based on the analysis of the region of $\Delta < 0$, we see that when $\tilde{q}_- < \tilde{q}_l < \tilde{q}_+$, the critical wavenumber $\tilde{q}^*$ can be $\tilde{q}_-$, $\tilde{q}_+$, or $\tilde{q}_l$, whichever makes $\Delta(\tilde{q}^*) = 0$ at the smallest Pe_C'. In all other cases, including when $\tilde{q}_{l,r}$ do not exist ($\text{Da} > (\alpha + 1)^2/12\alpha$), $\tilde{q}^*$ can only be $\tilde{q}_-$, $\tilde{q}_+$, whichever makes $\Delta(\tilde{q}^*) = 0$ at the smallest Pe_C'. Therefore, we define the Péclet number Pe_C' that corresponds to $\Delta(\tilde{q}_\pm) = 0$,

$$\text{Pe}_{C,\pm}' = \frac{(\tilde{\mathcal{M}} - \tilde{\mathcal{D}})^2(\tilde{q}_\pm^2)}{4\alpha^{-1}\text{Da}\tilde{q}_\pm^2} = \frac{(\tilde{q}_\pm^2 + \text{Da})^2}{\alpha\text{Da}\tilde{q}_\pm^2}. \tag{S59}$$

In summary, when $\alpha > \alpha_{\text{crit}}$, the unstable modes become oscillatory when $\text{Pe}_C' > \text{Pe}_{C,*}'$, where

$$\text{Pe}_{C,*}' = \begin{cases} \min\{\text{Pe}_{C,+}', \text{Pe}_{C,-}', \text{Pe}_{C,l}'\} \text{ when} \\ \quad \text{Da} < (\alpha + 1)^2/12\alpha, \\ \quad \text{Da} > 1 - 2/\alpha, \\ \quad \text{and } \alpha > 5 \\ \min\{\text{Pe}_{C,+}', \text{Pe}_{C,-}'\} \text{ otherwise.} \end{cases} \tag{S60}$$

Therefore, we have established that oscillatory instability occurs when chemoattractant diffusion is slow and chemotaxis is sufficiently fast.

Lastly, we note that by setting $\text{Pe}_{C,+}' = \text{Pe}_{C,-}'$, we find further that when $\alpha\text{Da} < 1$, $\text{Pe}_{C,+}' < \text{Pe}_{C,-}'$, and when $\alpha\text{Da} \geq 1$, $\text{Pe}_{C,+}' \geq \text{Pe}_{C,-}'$.

E. Linear stability outside the MIPS spinodal

Outside the MIPS spinodal region where the free energy is convex, or $\partial_\phi\tilde{\mu}_h > 0$. We see from Eq. (S32) that the sum of the eigenvalues is

$$\omega_+ + \omega_- = -(\mathcal{M} + \mathcal{D}),$$
$$\omega_+ + \omega_- = -(Mq^2(\partial_\phi\tilde{\mu}_h + \kappa q^2) + D_c q^2 + k\phi_0 g'). \tag{S61}$$

Because $\partial_\phi \tilde{\mu}_h > 0$ and $g' > 0$, we have $\omega_+ + \omega_- \leq 0$, and the product of the eigenvalues is

$$\omega_+ \omega_- = \mathcal{MD} + \mathcal{X},$$
$$\omega_+ \omega_- = Mq^2(\partial_\phi \tilde{\mu}_h + \kappa q^2)(D_c q^2 + k\phi_0 g') + k\chi_0 \phi_0 f' g q^2. \tag{S62}$$

Because for chemoattractant $\chi_0 > 0$, we have $\omega_+ \omega_- \geq 0$. Therefore Re $\omega_\pm \leq 0$ and the homogeneous state is stable.

S4. LINEAR STABILITY ANALYSIS IN THE $\text{Pe}_R - \phi_0$ PHASE DIAGRAM

The results of linear stability analysis in §S3 are described in terms of the three dimensionless parameters α, Da, and Pe'_C. In their expressions (Eq. S39), $\partial_\phi \tilde{\mu}_h$ is a function of ϕ_0 and Pe_R, and M is a function of ϕ_0. ϕ_0 and Pe_R are the two dimensionless parameters in the conventional MIPS phase diagram. Therefore, in the main text, we define another version of the parameters that do not involve any dependence on ϕ_0 and Pe_R: α_0, Da_0 and Pe_C. Using linear models for chemotactic sensing function and chemoattractant rate $f(\tilde{c}) = \tilde{c}$ and $g(\tilde{c}) = \tilde{c}$, the two versions of dimensionless parameters are related by

$$\alpha = -\phi_0(\partial_\phi \tilde{\mu}_h)\alpha_0,$$
$$\text{Da} = -\frac{\phi_0}{\partial_\phi \tilde{\mu}_h}\text{Da}_0, \tag{S63}$$
$$\text{Pe}'_C = \text{Pe}_C \frac{S}{k} \cdot \frac{(-1)}{\phi_0^2 \partial_\phi \tilde{\mu}_h}.$$

Fig. 2 in the main text shows the chemotactic MIPS phase diagram in the plane of $\text{Pe}_C - \alpha_0$ at given Da_0, ϕ_0 and Pe_R. The linear stability analysis results can be easily applied using the conversion in Eq. (S63).

Fig. 1 in the main text shows the chemotactic MIPS phase diagram in the plane of $\text{Pe}_R - \phi_0$ at given α_0, Da_0, and Pe_C. In this phase diagram, we would like to obtain the stability criteria and different types of instabilities expressed in terms of Pe_R and ϕ_0, which we derive in this section.

When there is no chemotaxis, the stability boundary is the spinodal curve $\partial_\phi \tilde{\mu}_h(\phi_0, \text{Pe}_{R,\text{sp}}) = 0$. Using Eq. (S5), the spinodal curve can be written explicitly in terms of Pe_R:

$$\text{Pe}_{R,\text{sp}} = \frac{\pi(\phi_0 - \phi_m)^2(\phi_0^{-1} - 2 - 0.6\phi_0)}{4\phi_m(\phi_0 - 2\phi_m)}. \tag{S64}$$

Because $\partial_\phi \tilde{\mu}_h$ is linear with respect to Pe_R, in the following text, we give the stability and instability type conditions in terms of $\partial_\phi \tilde{\mu}_h$; the expression can then be easily written explicitly in terms of Pe_R. Based on Eq. (S64), because $\text{Pe}_{R,\text{sp}} > 0$ and $0 < \phi_0 < \phi_m$, we have $\phi_0^{-1} - 2 - 0.6\phi_0 < 0$. Hence, we find that the spinodal curve spans the range of volume fractions given by $(-5 + 2\sqrt{10})/3 < \phi_0 < \phi_m$.

Based on Eq. (S42), the criterion (1) ($\text{Pe}'_C \geq \text{Pe}'_{C\text{crit}}$) can be written in terms Pe_C, Da_0, ϕ_0, and $\partial_\phi \tilde{\mu}_h$ as

$$\frac{S}{k} \cdot \text{Pe}_C \geq \phi_0^3 \begin{cases} -\partial_\phi \tilde{\mu}_h/\phi_0, & \text{for } (-\mu'_h/\phi_0 \leq \text{Da}_0) \\ \frac{(\text{Da}_0 - \partial_\phi \tilde{\mu}_h \phi_0^{-1})^2}{4\text{Da}_0}, & \text{for } (-\mu'_h/\phi_0 > \text{Da}_0) \end{cases}, \tag{S65}$$

or explicitly in terms of $\partial_\phi \tilde{\mu}_h$:

$$-\frac{\partial_\phi \tilde{\mu}_h}{\phi_0} \leq \begin{cases} \frac{S\text{Pe}_C}{k\phi_0^3}, & \text{for } (\frac{S\text{Pe}_C}{k\phi_0^3} < \text{Da}_0) \\ 2\sqrt{\frac{S\text{Pe}_C}{k\phi_0^3}\text{Da}_0} - \text{Da}_0, & \text{otherwise.} \end{cases} \tag{S66}$$

Thus we have also obtained the expression for Boundary 1 in the $\text{Pe}_R - \phi$ phase diagram by setting Eq. (S66) to equality, and the region above Boundary 1 satisfies criterion (1).

Similarly, criterion (2) ($\alpha \leq 1$ or $\text{Da} \geq (\alpha - 1)^2/4\alpha$) can be written in terms of α_0, Da_0, ϕ_0, and $\partial_\phi \tilde{\mu}_h$ as

$$-\partial_\phi \tilde{\mu}_h \leq \frac{1}{\phi_0 \alpha_0}\left(1 + 2\phi_0\sqrt{\text{Da}_0 \alpha_0}\right). \tag{S67}$$

Thus we have also obtained the expression for Boundary 2 in the $\text{Pe}_R - \phi$ phase diagram by setting Eq. (S67) to equality, and the region above Boundary 2 satisfies criterion (2).

Finite-wavelength instability $\text{Pe}'_C > 1$ can be expressed as

$$-\partial_\phi \tilde{\mu}_h < \frac{S\text{Pe}_C}{k\phi_0^2}, \tag{S68}$$

which coincides with criterion (1) if $S\text{Pe}_C/(k\phi_0^3) < \text{Da}_0$. Setting Eq. (S68) to equality gives the expression for the F/U boundary. Finite-wavelength instability exists between the F/U boundary and Boundary 1 when $S\text{Pe}_C/(k\phi_0^3) > \text{Da}_0$.

Finally, oscillatory instability occurs when $\text{Pe}'_C > \text{Pe}'_{C,*}$ and $\alpha > \alpha_{\text{crit}}$. The following derivation needs to be discussed separately depending on whether $\text{Da} < (\alpha + 1)^2/12\alpha$, $\text{Da} > 1 - 2/\alpha$, and $\alpha > 5$, which is equivalent to

$$\max\{5, \phi_0\sqrt{12\alpha_0\text{Da}_0} - 1\} < \alpha < 2 + \phi_0^2\alpha_0\text{Da}_0. \tag{S69}$$

If outside this region, the condition for oscillatory unstable mode is $\text{Pe}'_C > \min\{\text{Pe}'_{C,+}, \text{Pe}'_{C,-}\}$, which is equivalent to

$$P \equiv 2\text{Pe}_C \frac{S}{k}\alpha_0^2\text{Da}_0\phi_0 > \min\{h(u_+), h(u_-)\}, \tag{S70}$$

where

$$h(u) = \frac{(u + 2\alpha\text{Da})^2}{u}, \tag{S71}$$

and

$$u_\pm = \alpha - 1 \pm \sqrt{(\alpha - 1)^2 - 4\alpha\text{Da}}. \tag{S72}$$

Because

$$h(u) \geq 8\alpha \mathrm{Da}, \qquad (S73)$$

and the equality is attained at $u = 2\alpha \mathrm{Da}$, this puts a lower bound on Pe_C:

$$\mathrm{Pe}_C \frac{S}{k} > \frac{4\phi_0}{\alpha_0}. \qquad (S74)$$

Given the above constraint, the roots of $P = h(u)$ are

$$u^{\pm} = \frac{1}{2}\left[P - 4\alpha\mathrm{Da} \pm \sqrt{P^2 - 8\alpha\mathrm{Da}P} \right]. \qquad (S75)$$

Hence, Eq. (S70) is equivalent to $u^- < u_+ < u^+$ or $u^- < u_- < u^+$, that is, at least one of $u_{\pm}$ is in between the two roots $u^{\pm}$. Recall that we would like to express the condition of oscillatory instability in terms of $\partial_\phi \tilde\mu_h$ explicitly. Because $\alpha\mathrm{Da} = \alpha_0\mathrm{Da}_0\phi_0^2$, $u^{\pm}$ does not depend on $\partial_\phi \tilde\mu_h$. But $u_{\pm}$ depends on $\partial_\phi \tilde\mu_h$ because of α. Our goal, then, is to express $u^- < u_+ < u^+$ or $u^- < u_- < u^+$ explicitly in terms of α, from which we obtain the condition in terms of $\partial_\phi \tilde\mu_h$ via $\partial_\phi \tilde\mu_h = -\alpha/(\alpha_0\phi_0)$.

To achieve the above goal, we first notice that

$$\alpha - 1 = j(u_{\pm}) \equiv \frac{u_{\pm}^2 + 4\alpha\mathrm{Da}}{2u_{\pm}}. \qquad (S76)$$

The following derivation uses the property that the minimum of $h(u)$ is obtained at $u = 2\alpha\mathrm{Da}$ and the minimum of $j(u)$ is obtained at $u = 2\sqrt{\alpha\mathrm{Da}}$.

We first consider condition (a) $2\sqrt{\alpha\mathrm{Da}} \leq u^- < u^+$. Because $h(u^-) = P$, this requires: $2\alpha\mathrm{Da} \geq 2\sqrt{\alpha\mathrm{Da}}$, or $\alpha\mathrm{Da} \geq 1$ (which corresponds to $\mathrm{Pe}'_{C,+} > \mathrm{Pe}'_{C,-}$ as noted in § S8), and $P \leq h(2\sqrt{\alpha\mathrm{Da}})$, or

$$P \leq 2\sqrt{\alpha\mathrm{Da}}(\sqrt{\alpha\mathrm{Da}} + 1)^2. \qquad (S77)$$

Under condition (a), $u^- < u_+ < u^+$ or $u^- < u_- < u^+$ is equivalent to $j(u^-) < \alpha - 1 < j(u^+)$.

Next, we consider condition (b) $u^- < u^+ \leq 2\sqrt{\alpha\mathrm{Da}}$, which requires $\alpha\mathrm{Da} \leq 1$ and Eq. (S77), then $u^- < u_+ < u^+$ or $u^- < u_- < u^+$ is equivalent to $j(u^+) < \alpha - 1 < j(u^-)$.

Lastly, if (c) $u^- < 2\sqrt{\alpha\mathrm{Da}} < u^+$, which requires $P > h(2\sqrt{\alpha\mathrm{Da}})$, or the opposite of Eq. (S77), then $u^- < u_+ < u^+$ or $u^- < u_- < u^+$ is equivalent to $2\sqrt{\alpha\mathrm{Da}} < \alpha - 1 < \max\{j(u^-), j(u^+)\}$, where the lower bound is the minimum of $j(u)$ ($\min_u j(u) = 2\sqrt{\alpha\mathrm{Da}}$). Notice that $\alpha - 1 > 2\sqrt{\alpha\mathrm{Da}}$ is equivalent to $\mathrm{Da} < (\alpha-1)^2/4\alpha$. Hence all conditions above imply $\mathrm{Da} < \mathrm{Da}_{\mathrm{crit}}$ (or $\alpha > \alpha_{\mathrm{crit}}$).

Now we have obtained the condition of oscillatory instability in terms of α and hence $\partial_\phi \tilde\mu_h$ explicitly, which has an upper and lower bound. The upper bound coincides with or is below Boundary 2.

In summary, in this section, we have derived the conditions for stability or instability (both type F/U and type S/O) in the $\mathrm{Pe}_R - \phi_0$ phase diagram, by expressing them explicitly in terms of $\partial_\phi \tilde\mu_h$.

S5. NUMERICAL SIMULATIONS

In this section, we describe the details of numerical simulations. Firstly, we define the characteristic length scale to be $l_0 \equiv \sqrt{\kappa} \sim U_0\tau_R$, which is on the order of the persistence length [3, 7]. We define the characteristic time scale to be $t_0 \equiv \kappa/M_0 \sim \tau_R$, which is on the order of the ABP reorientation time. The characteristic length and time scales motivate us to define the characteristic velocity $u_0 \equiv l_0/t_0 \sim U_0$, which we will use in § S8.

All simulations in this work are performed in a periodic domain of size $[100l_0, 100l_0]$. The governing equations are solved using the finite volume method to ensure conservation of particle volume fraction and chemoattractant concentration. We use an implicit solver of variable order as the time-stepper with adaptive time stepping, adaptive order and error control [10]. Simulations are solved on a grid of size $[256, 256]$. The initial condition for $\phi(x, t = 0)$ is the homogeneous state ϕ_0 with added spatially uncorrelated Gaussian noise at each grid point with a standard deviation of 0.02. The initial condition for the chemoattractant concentration is the homogeneous state $\tilde c(x, t = 0) = \tilde c_0 = S/(k\phi_0)$ which satisfies the steady state condition.

Snapshots in Fig. 1 and Fig. 2 in the main text are taken at $t = 4 \times 10^4 t_0$ and $t = 2 \times 10^4 t_0$, respectively. Note that in Fig. 2(b-c), of the two eigenvalues, only the higher one $\tilde\omega_+$ is shown since it determines the stability. In all phase diagrams where simulations are displayed (Fig. 1-2, SI Movie 1-7), the parameters for the simulations correspond to the coordinates of the center of the images.
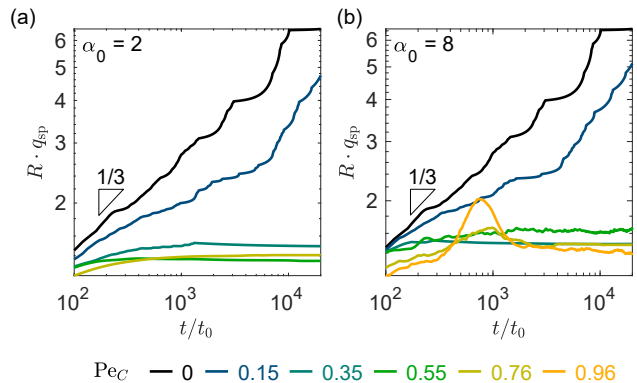
S6. CHARACTERIZATION OF COARSENING DYNAMICS

FIG. S2: Evolution of the characteristic domain sizes that correspond to the simulations at $\alpha_0 = 2$ and 8 and increasing values of Pe_C in Fig. 2(a) in the main text.

It is known that in conventional MIPS the size of phase-separated domain coarsens over time [3]. However,

as shown in the main text, chemotaxis can arrest such coarsening. In this section, we quantify the coarsening dynamics by plotting the evolution of the characteristic domain size over time, defined to be [11–13]

$$R(t) = \left[\frac{\int |\boldsymbol{q}| \mathcal{S}(\boldsymbol{q}, t) d\boldsymbol{q}}{\int \mathcal{S}(\boldsymbol{q}, t) d\boldsymbol{q}} \right]^{-1}, \qquad \text{(S78)}$$

where $\mathcal{S}(\boldsymbol{q}, t)$ is the structure factor associated with spatial variations in particle volume fraction

$$\mathcal{S}(\boldsymbol{q}, t) = |\Delta \hat{\phi}(\boldsymbol{q}, t)|^2, \qquad \text{(S79)}$$

where $\Delta \hat{\phi}$ is the Fourier transform of $\Delta \phi = \phi - \phi_0$.

Fig. S2(a-b) shows the normalized characteristic domain size $R q_{\rm sp}$ with respect to time that correspond to the simulations with $\alpha_0 = 2$ and 8 in Fig. 2(a) in the main text ($\mathrm{Da}_0 = 0.5$, $\mathrm{Pe}_R = 10^{-3}$, $\phi = 0.8$). The domain size of the case of non-chemotactic MIPS ($\mathrm{Pe}_C = 0$) grows as $R \sim t^{1/3}$ (black curve), consistent with the growth law of spinodal decomposition [14], showing that the coarsening persists. With increasing Pe_C, this coarsening slows down (blue to chartreuse curves), eventually becomes arrested and gives rise instead to finite-sized domains characteristic of a Type F instability.

Next, we show more examples of the coarsening dynamics with smaller steps of increasing Pe_C. Fig. S3 shows the snapshots of the coarsening process and the dependence on Pe_C when $\mathrm{Da}_0 = 0.5$, $\mathrm{Pe}_R = 10^{-3}$, $\phi = 0.8$ and $\alpha_0 = 2$ and 10, along with the corresponding $R(t)$. Pe_C is chosen such that it is equally spaced between 0 and 90% of the critical Pe_C that corresponds to Boundary 1. We see that when the patterns are stationary ($\alpha_0 = 2$), with increasing Pe_C, the coarsening generally slows down, and the domain size at steady state decreases. For $\alpha_0 = 10$, coarsening also slows down with increasing Pe_C until the pattern becomes oscillatory, when initially, the coarsening may be faster than stationary patterns. Note that $R(t)$ is typically non-monotonic for oscillatory patterns, and when $R(t)$ converges to a steady value at longer time, the steady value decreases with increasing Pe_C.

The observation above can also be seen in Fig. S4, which shows the results for $\phi_0 = 0.65$ (other dimensionless parameters are identical to Fig. S3). Because the pattern for $\phi_0 = 0.65$ is bicontinuous for a larger fraction of the time, at $\mathrm{Pe}_C = 0$, the growth curve $R(t)$ is smoother than $\phi_0 = 0.8$ shown in Fig. S2, which shows step increase due to events of dissolution and merger of phases. Again, we confirm the $R \sim t^{1/3}$ power law for non-chemotactic MIPS ($\mathrm{Pe}_C = 0$). In the main text, we referred the readers to Figs. S3 and S4 for snapshots of the non-chemotactic spinodal decomposition.

Fig. S4 also shows that the slope of $\ln R - \ln t$ decreases with increasing Pe_C for stationary patterns at both $\alpha_0 = 2$ and 10, again indicating slower coarsening. A traveling pattern is instead observed at $\alpha_0 = 10$ and $\mathrm{Pe}_C = 0.39$, for which $R(t)$ shows non-monotonic behavior.
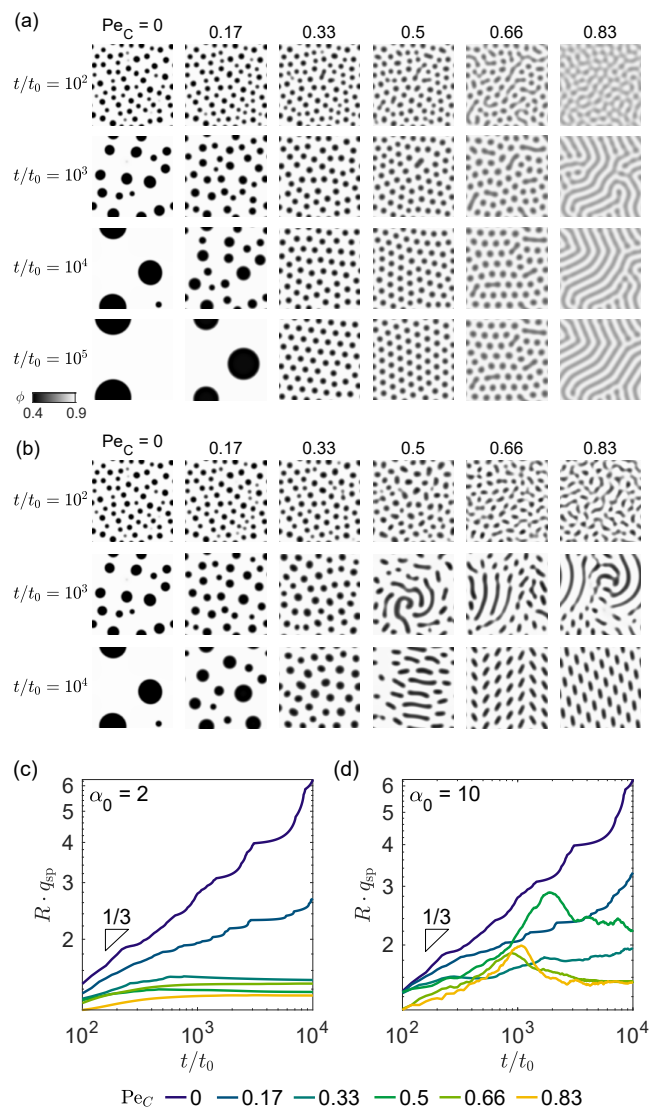

FIG. S3: (a-b) Snapshots of simulations and (c-d) evolution of the characteristic domain size $R(t)$ at $\mathrm{Da}_0 = 0.5$, $\mathrm{Pe}_R = 10^{-3}$, $\phi_0 = 0.8$, $\alpha_0 = 2$ (a,c) and 10 (b,d), and increasing values of Pe_C.

S7. CHARACTERIZATION OF SMALL-AMPLITUDE FLUCTUATION

In this section, we verify the classification of type F/U instability based on the linear stability analysis using numerical simulations. To compare with the dispersion relation shown in Fig. 2(b-c) in the main text, we perform simulations at these parameters. The initial condition for $\phi(x)$ is a homogeneous ϕ_0 with added spatially uncorrelated Gaussian noise at each grid point with a standard deviation of 0.001. We use a small amplitude perturbation here to reduce the nonlinear effect. The initial condition for the chemoattractant concentration is the homogeneous state $\tilde{c}(x, t = 0) = \tilde{c}_0 = S/(k\phi_0)$
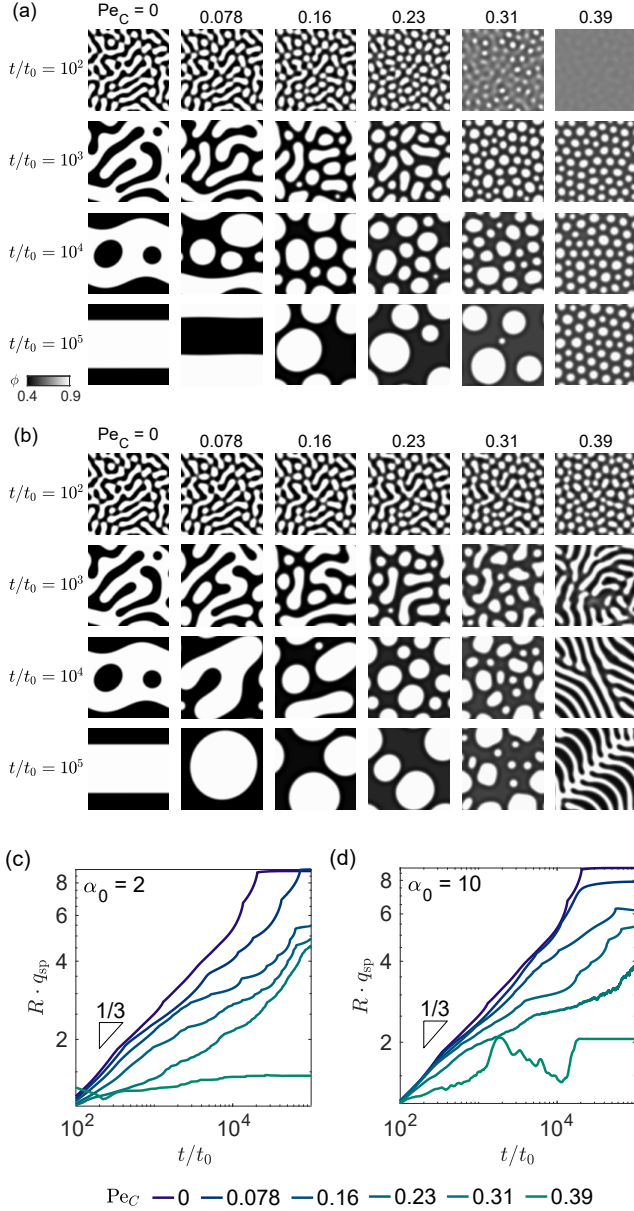
FIG. S4: (a-b) Snapshots of simulations and (c-d) evolution of the characteristic domain size $R(t)$ at $\mathrm{Da}_0 = 0.5$, $\mathrm{Pe}_R = 10^{-3}$, $\phi_0 = 0.65$ for $\alpha_0 = 2$ (a,c) and 10 (b,d).
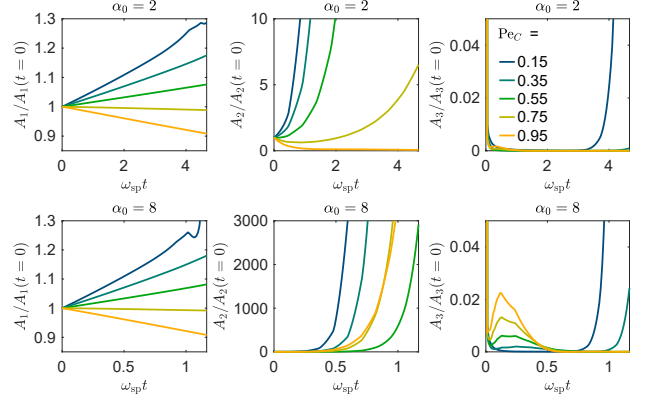

FIG. S5: The time evolution of the perturbation in the long (A_1), medium (A_2) and short wavelength (A_3) regimes. The parameters correspond to the columns of $\alpha_0 = 2$ and $\alpha_0 = 8$ in Fig. 2(a) in the main text.

and $\mathrm{Pe}_C = 0.95$ correspond to type F and other cases correspond to type U. In the medium wavelength regime where the instability grows the fastest, the perturbation grows for all cases except for $\alpha_0 = 2$ and $\mathrm{Pe}_C = 0.95$, which is linearly stable at all wavelengths. Note that the curve is nonmotonic for $\alpha_0 = 2$ and $\mathrm{Pe}_C = 0.75$. This can be due to the coupling between ϕ and c, since the perturbation we impose is not an eigenvector in the linear stability analysis. In the short wavelength regime, initially all amplitudes decrease sharply.

S8. CHARACTERIZATION OF OSCILLATORY PATTERN FORMATION

In Fig. 2(a) in the main text, we plot the velocity (red arrows) of the patterns. In this section, we show the definition of the velocity and its dependence on Pe_C and α_0.

To quantify the velocity of stripes that span the entire domain and spirals, we define a level set velocity $\boldsymbol{u}$, that is, the velocity at which contours of ϕ move in the direction along the gradient: $\boldsymbol{u} = -\partial_t \phi \cdot \nabla\phi / |\nabla\phi|^2$. Note that the level set velocity is undefined when the gradient vanishes. Cases that use this definition are: $\mathrm{Pe}_C = 0.96$, $\alpha_0 = 4, 6, 8, 10$, and $\mathrm{Pe}_C = 0.76$, $\alpha_0 = 10$. For all other cases, which exhibit dot-like and short stripe-like patterns, $\boldsymbol{u}$ is instead defined to be the velocity of the center of mass of each of the disjoint regions defined by $\{x | \phi(x) < 0.7\}$ to facilitate ease of visualization. The vectors of $\boldsymbol{u}$ are indicated by the red arrows in Fig. 2(a). The scale bar $u_0 \equiv l_0/t_0 \sim U_0$ indicates the characteristic velocity.

Fig. S6 summarizes the velocity of patterns shown in Fig. 2(a). We compute the average speed $\overline{\boldsymbol{u}}$ at $t/t_0 = 2 \times 10^4$. The level set velocity is averaged over all grid points for which $|\nabla\phi| > 0.03 l_0^{-1}$ to avoid inaccuracy when the magnitude of the gradient is small (level set velocity

with added noise that has the opposite sign as the added noise for $\phi(x)$. We observe the early time evolution of long, medium, and short wavelength modes by defining the following quantities based on the structure factor: $A_1(t) = \int_0^{0.16 q_{\mathrm{sp}}} S(\boldsymbol{q}, t) d\boldsymbol{q}$, $A_2(t) = \int_{0.5 q_{\mathrm{sp}}}^{q_{\mathrm{sp}}} S(\boldsymbol{q}, t) d\boldsymbol{q}$, $A_3(t) = \int_{\sqrt{2} q_{\mathrm{sp}}}^{\infty} S(\boldsymbol{q}, t) d\boldsymbol{q}$. Fig. S5 shows that in the long wavelength regime for both $\alpha_0 = 2$ and $\alpha_0 = 8$, the amplitude of the perturbation decreases for $\mathrm{Pe}_C = 0.75$ and 0.95 and increases for other cases, consistent with the dispersion relation in Fig. 2(b-c), verifying that $\mathrm{Pe}_C = 0.75$
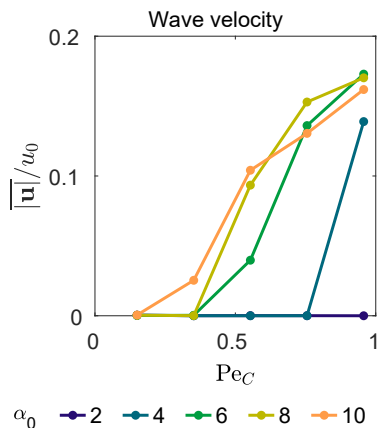
FIG. S6: Average speed of patterns corresponding to Fig. 2(a) in the main text.

is undefined when $|\nabla\phi| = 0$), while the center of mass velocity is averaged over all disjoint regions. We see that patterns move faster with increasing Pe_C and the onset of motion occurs at lower Pe_C with increasing α_0.

As a reference, the average speed of the patterns at $\text{Pe}_C = 0.95$ is on the order of $0.1u_0$, which means that the pattern travels at a speed that is an order of magnitude smaller than the speed at which ABP particles self-propel.

S9. APPLICATION IN LIVING AND SYNTHETIC SYSTEMS

In this section, we estimate the values of the dimensionless parameters of living systems and discuss ways to study the phase diagram of chemotactic MIPS experimentally by tuning certain properties of synthetic colloidal systems.

Populations of motile bacteria. We use *Myxococcus xanthus* and *Escherichia coli* as representative examples to draw estimates of parameter values from. $\text{Pe}_R \sim 10^{-2}$, and hence, cells may undergo MIPS at sufficiently high cell density [15]. We therefore take $\partial_\phi\tilde\mu_h \sim 1$ as shown in Eq. (S6) for cells in the spinodal region of MIPS. The experimentally measured diffusivity M_0 can range from ~ 0.1 to $\sim 10^2$ $\mu m^2/s$ [15–17], typically lower than chemoattractant diffusivity, which suggests that $\alpha \lesssim 1$. The typical chemoattractant depletion length is $\sqrt{D_c/k} \sim 1$ µm [16], and persistence length l_0 [18] is about 20 µm, hence $\text{Da} \sim 10^2$. These estimates suggest that populations of motile bacteria satisfy criterion (2), indicating that MIPS can be suppressed by chemotaxis when $\text{Pe}'_C \approx \text{Pe}_C \cdot S/k$ is sufficiently large. Because $\text{Pe}_C \sim 10$ [16, 17, 19], when chemoattractant is abundant (S is large), MIPS is suppressed. Conversely, when chemoattractant is limited, we expect that MIPS can occur.

For synthetic systems such as self-propelled colloids,

because $\text{Da} \sim U_0^2\tau_R^2 k/D_c$, and $\alpha \sim U_0^2\tau_R/D_c$, Da and α can be tuned via the swimming velocity U_0 e.g., using external stimuli such as light [20–23]. In addition, Da can be tuned by changing the reactive material to alter the chemoattractant uptake rate k. Finite-sized domains arise experimentally if synthetic chemotactic colloids have a low uptake rate k, which leads to smaller Da. With a smaller Da and a larger α (such as by increasing U_0), oscillatory dynamics involving clusters of colloidal particles traveling in space may arise.

S10. POSSIBLE EXTENSIONS OF OUR WORK

The derivation in § S2 indicates that our continuum model is a suitable description for the long time and length scale dynamics of chemotactic ABPs that self-propel and undergo chemotactic drift and alignment—and thus is broadly applicable to many living and active systems. While we focused on the case in which the particles are attracted to and consume the chemical signal, our conclusions also hold for the case in which the particles are *repelled by ($\chi_0 < 0$) and produce* the chemical signal. This case also allows for a homogeneous steady state around which a linear stability analysis can be easily performed, exactly following the procedure described in above, yielding similar behavior to that described in this paper. Intuitively, this can be understood as arising because in both forms of chemotaxis, the chemical gradient generated by particle consumption or production causes the particles to disperse, which competes against motility-induced phase separation.

Nevertheless, there are many other different ways in which chemotaxis can arise, possibly leading to different types of couplings in the continuum theory; exploring these other forms of chemotaxis will be an important future direction for research, building on our work. For example, the effective free energy may depend on the chemoattractant concentration gradient. By not having the chemoattractant concentration gradient in the free energy, our model is the lowest order model that couples chemotaxis and MIPS in an additive way. Exploring other forms of chemotaxis, leading to other more complex forms of Eq. (2) in the main text, will be an important future direction for research, building on our work.

In addition, in contrast to the illustrative case considered here, producers of a chemoattractant or consumers of a chemorepellent are attracted to each other by chemotaxis and aggregate, hence further enhancing phase separation, resulting in fundamentally different behaviors. In such cases, chemotaxis can give rise to pattern formation without requiring MIPS: for example, when the individual active agents produce a chemoattractant (which is the case for e.g., the aggregation of the slime mold *Dictyostelium discoideum*) or conversely consume a chemorepellent. Exploring the interplay between MIPS and these other forms of chemotaxis using the approach we developed will surely be a fascinating direction for future work.

Variable	Physical meaning
a	ABP particle radius
U_0	ABP self-propulsion speed
τ_R	ABP reorientation time
$M_0 = \frac{1}{2}U_0^2\tau_R$	ABP active diffusivity
ϕ_0	Average ABP volume fraction
$\tilde{\mu}_h$	Normalized ABP chemical potential
$l_0 \equiv \sqrt{\kappa} \sim U_0\tau_R$	Characteristic length scale of the width of the MIPS interface
D_c	Chemoattractant diffusivity
k	Chemoattractant uptake rate coefficient
S	Chemoattractant supply rate
χ_0	Chemotactic coefficient
$f(\tilde{c}) = \tilde{c}$	Chemotactic sensing function
$g(\tilde{c}) = \tilde{c}$	Dependence of chemoattractant uptake rate on chemoattractant concentration
$\mathrm{Pe}_R \equiv \frac{a}{U_0\tau_R}$	Reorientational Péclet number: directedness of ABPs
$\alpha_0 \equiv \frac{M_0}{D_c}$	Ratio of single-particle ABP to chemoattractant diffusivity
$\mathrm{Da}_0 \equiv \frac{\kappa k}{D_c}$	Chemoattractant uptake rate to diffusion rate over $\sqrt{\kappa}$
$\mathrm{Pe}_C \equiv \frac{\chi_0}{M_0}$	Chemotactic Péclet number: ratio of ABP chemotactic coefficient to diffusivity
$\alpha \equiv \frac{-M_0\phi_0\partial_\phi\tilde{\mu}_h}{D_c} = -\alpha_0\phi_0\partial_\phi\tilde{\mu}_h$	Ratio of effective collective ABP to chemoattractant diffusivity
$\mathrm{Da} \equiv -\frac{\kappa k\phi_0 g'}{D_c\partial_\phi\tilde{\mu}_h} = -\mathrm{Da}_0\frac{\phi_0 g'}{\partial_\phi\tilde{\mu}_h}$	Damköhler number: effective chemoattractant uptake to diffusion rate
$\mathrm{Pe}_C' \equiv -\frac{\chi_0}{M_0\phi_0\partial_\phi\tilde{\mu}_h}\frac{f'g}{g'} = -\mathrm{Pe}_C\frac{f'g}{\phi_0\partial_\phi\tilde{\mu}_h g'}$	Reduced chemotactic Péclet number: effective ABP chemotactic to diffusivity rate

TABLE S1: Summary of variables and dimensionless parameters.

We also note the confusing point that Keller and Segel — whose 1971 paper forms the basis of our model of chemotaxis — also published another seminal but distinct model of chemotaxis [24] that is suitable to the case of slime mold aggregation noted above. Examining the interplay between MIPS and this alternative version of the Keller-Segel model could be an interesting way to extend our work.

More broadly, while we focused on biased motion up a chemoattractant gradient as an illustrative example, our theoretical framework also provides a foundation to describe the influence of other forms of taxis—e.g., durotaxis, electrotaxis, and phototaxis [25–32]—on MIPS. Moreover, while we focused on a specific model of MIPS, extending our framework to other forms of active phase separation (e.g., [33–39]) would be interesting.

Finally, as noted above and in the main text, it is important to note that while our linear stability analysis provides useful predictions for the boundary of stability, it is not accurate in predicting more complex nonlinear features such as the boundary between arrested coarsening and patterns that coarsen. While the prediction of finite or unbounded wavelength instability based on the linear stability analysis can be verified through simulations by tracking the amplitude of perturbations at short, medium, and long wavelengths over time at early times not far from the homogeneous state, it does not quantitatively predict whether the pattern coarsens as the system reaches deeper into the nonlinear regime at longer time scales. Therefore, we use linear stability analysis only to provide an approximate explanation of the essential physics underlying finite wavelength selection and the observation of finite-sized domains that do not coarsen, which becomes more common with increasing chemotactic rate. More accurate quantitative agreement will require nonlinearities to be explicitly incorporated in the analysis.

S11. SUPPLEMENTARY MOVIES

1. Animated profiles of $\phi(\boldsymbol{x})$ that show non-chemotactic MIPS in the $\mathrm{Pe}_R - \phi_0$ phase diagram ($\mathrm{Pe}_C = 0$).

2. Animated profiles of $\phi(\boldsymbol{x})$ for the simulations in Fig. 1(b). $\mathrm{Da}_0 = 0.2$, $\alpha_0 = 1$, $\mathrm{Pe}_C = 1$.

3. Animated profiles of $\phi(\boldsymbol{x})$ for the simulations in Fig. 1(d). $\mathrm{Da}_0 = 0.2$, $\alpha_0 = 4$, $\mathrm{Pe}_C = 1$.

4. Animated profiles of $\phi(\boldsymbol{x})$ for the simulations in Fig. 1(f). $\mathrm{Da}_0 = 0.5$, $\alpha_0 = 10$, $\mathrm{Pe}_C = 0.35$.

5. Animated profiles of $c(\boldsymbol{x})$ for the simulations in Fig. 1(b). $\mathrm{Da}_0 = 0.2$, $\alpha_0 = 1$, $\mathrm{Pe}_C = 1$.

6. Animated profiles of $c(\boldsymbol{x})$ for the simulations in Fig. 1(d). $\mathrm{Da}_0 = 0.2$, $\alpha_0 = 4$, $\mathrm{Pe}_C = 1$.

7. Animated profiles of $\phi(\boldsymbol{x})$ for the simulations in Fig. 2(a). $\mathrm{Da}_0 = 0.5$, $\mathrm{Pe}_R = 10^{-3}$, $\phi_0 = 0.8$.

[1] S. C. Takatori and J. F. Brady, Towards a thermodynamics of active matter, Physical Review E **91**, 032117 (2015).

[2] M. E. Cates and J. Tailleur, When are active brownian particles and run-and-tumble particles equivalent? consequences for motility-induced phase separation, EPL (Europhysics Letters) **101**, 20010 (2013).

[3] J. Stenhammar, A. Tiribocchi, R. J. Allen, D. Marenduzzo, and M. E. Cates, Continuum theory of phase separation kinetics for active brownian particles, Physical Review Letters **111**, 145702 (2013).

[4] O. Pohl and H. Stark, Dynamic clustering and chemotactic collapse of self-phoretic active particles, Physical Review Letters **112**, 238303 (2014).

[5] H. Stark, Artificial chemotaxis of self-phoretic active colloids: Collective behavior, Accounts of Chemical Research **51**, 2681 (2018).

[6] J. Bialké, H. Löwen, and T. Speck, Microscopic theory for the phase separation of self-propelled repulsive disks, EPL **103**, 10.1209/0295-5075/103/30008 (2013).

[7] M. E. Cates and J. Tailleur, Motility-induced phase separation, Annual Review of Condensed Matter Physics **6**, 219 (2015).

[8] J. Tailleur and M. E. Cates, Statistical mechanics of interacting run-and-tumble bacteria, Physical Review Letters **100**, 218103 (2008).

[9] M. C. Cross and P. C. Hohenberg, Pattern formation outside of equilibrium, Reviews of Modern Physics **65**, 851 (1993).

[10] L. Shampine and M. Reichelt, Ode matlab solvers, Journal of Scientific Computing **18**, 1 (1997).

[11] H. Furukawa, Spinodal decomposition of two-dimensional fluid mixtures: A spectral analysis of droplet growth, Physical Review E - Statistical Physics, Plasmas, Fluids, and Related Interdisciplinary Topics **61**, 1423 (2000).

[12] M. Laradji, S. Toxvaerd, and O. G. Mouritsen, Molecular dynamics simulation of spinodal decomposition in three-dimensional binary fluids, Physical Review Letters **77**, 2253 (1996).

[13] S. Mao, D. Kuldinow, M. P. Haataja, and A. Košmrlj, Phase behavior and morphology of multicomponent liquid mixtures, Soft Matter **15**, 1297 (2019).

[14] A. J. Bray, Theory of phase-ordering kinetics, Advances in Physics **51**, 481 (2002).

[15] G. Liu, A. Patch, F. Bahar, D. Yllanes, R. D. Welch, M. C. Marchetti, S. Thutupalli, and J. W. Shaevitz, Self-driven phase transitions drive myxococcus xanthus fruiting body formation, Physical Review Letters **122**, 248102 (2019).

[16] R. Alert, A. Martínez-Calvo, and S. S. Datta, Cellular sensing governs the stability of chemotactic fronts, Physical Review Letters **128**, 148101 (2022).

[17] X. Fu, S. Kato, J. Long, H. H. Mattingly, C. He, D. C. Vural, S. W. Zucker, and T. Emonet, Spatial self-organization resolves conflicts between individuality and collective migration, Nature Communications **9**, 10.1038/s41467-018-04539-4 (2018).

[18] M. E. Cates, Diffusive transport without detailed balance in motile bacteria: Does microbiology need statistical physics?, Reports on Progress in Physics **75**, 10.1088/0034-4885/75/4/042601 (2012).

[19] T. Bhattacharjee, D. B. Amchin, J. A. Ott, F. Kratz, and S. S. Datta, Chemotactic migration of bacteria in porous media, Biophysj **120**, 3483 (2021).

[20] I. Buttinoni, G. Volpe, F. Kummel, G. Volpe, and C. Bechinger, Active brownian motion tunable by light, Journal of Physics Condensed Matter **24**, 10.1088/0953-8984/24/28/284129 (2012).

[21] J. Stenhammar, R. Wittkowski, D. Marenduzzo, and M. E. Cates, Light-induced self-assembly of active rectification devices, Science Advances **2**, 1 (2016).

[22] J. Arlt, V. A. Martinez, A. Dawson, T. Pilizota, and W. C. Poon, Painting with light-powered bacteria, Nature Communications **9**, 1 (2018).

[23] G. Frangipane, D. Dell'Arciprete, S. Petracchini, C. Maggi, F. Saglimbeni, S. Bianchi, G. Vizsnyiczai, M. L. Bernardini, and R. di Leonardo, Dynamic density shaping of photokinetic e. coli, eLife **7**, 1 (2018).

[24] E. F. Keller and L. A. Segel, Initiation of slime mold aggregation viewed as an instability, Journal of Theoretical Biology **26**, 399 (1970).

[25] P. Roca-Cusachs, R. Sunyer, and X. Trepat, Mechanical guidance of cell migration: lessons from chemotaxis, Current Opinion in Cell Biology **25**, 543 (2013).

[26] A. Shellard and R. Mayor, All roads lead to directional cell migration, Trends in Cell Biology **30**, 852 (2020).

[27] S. SenGupta, C. A. Parent, and J. E. Bear, The principles of directed cell migration, Nature Reviews Molecular Cell Biology **22**, 529 (2021).

[28] R. Sunyer, V. Conte, J. Escribano, A. Elosegui-Artola, A. Labernadie, L. Valon, D. Navajas, J. M. García-Aznar, J. J. Muñoz, P. Roca-Cusachs, and X. Trepat, Collective cell durotaxis emerges from long-range intercellular force transmission, Science **353**, 1157 (2016).

[29] R. Alert and J. Casademunt, Role of substrate stiffness in tissue spreading: Wetting transition and tissue durotaxis, Langmuir **35**, 7571 (2019).

[30] D. J. Cohen, W. J. Nelson, and M. M. Maharbiz, Galvanotactic control of collective cell migration in epithelial monolayers, Nature Materials **13**, 409 (2014).

[31] M. Mijalkov, A. McDaniel, J. Wehr, and G. Volpe, Engineering sensorial delay to control phototaxis and emergent collective behaviors, Physical Review X **6**, 011008 (2016).

[32] S. Palagi and P. Fischer, Bioinspired microrobots, Nature Reviews Materials **3**, 113 (2018).

[33] E. Sesé-Sansa, I. Pagonabarraga, and D. Levis, Velocity alignment promotes motility-induced phase separation, EPL **124**, 10.1209/0295-5075/124/30004 (2018).

[34] M. N. V. D. Linden, L. C. Alexander, D. G. Aarts, and O. Dauchot, Interrupted motility induced phase separation in aligning active colloids, Physical Review Letters **123**, 10.1103/PhysRevLett.123.098001 (2019).

[35] S. Saha, J. Agudo-Canalejo, and R. Golestanian, Scalar active mixtures: The nonreciprocal cahn-hilliard model, Physical Review X **10**, 041009 (2020).

[36] Z. You, A. Baskaran, and M. C. Marchetti, Nonreciprocity as a generic route to traveling states, Proceedings of the National Academy of Sciences **117**, 19767 (2020).

[37] A. Wysocki, R. G. Winkler, and G. Gompper, Propagating interfaces in mixtures of active and passive brownian particles, New Journal of Physics **18**, 123030 (2016).

[38] J. Zhang, R. Alert, J. Yan, N. S. Wingreen, and S. Granick, Active phase separation by turning towards regions of higher density, Nature Physics **17**, 961 (2021).

[39] S. Yin and L. Mahadevan, Contractility-induced phase separation in active solids, (2022).